CHALMERS
UNIVERSITY OF TECHNOLOGY

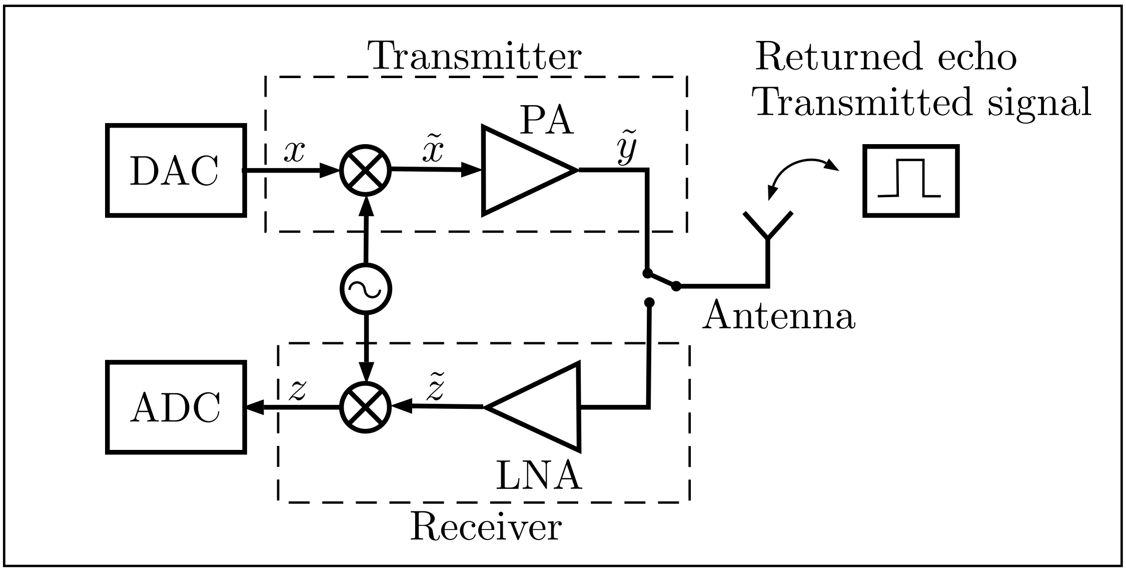

Pulse Shaping of Radar Transmitters

Compensation of Memory Effects through Digital Pre-distortion

Master's thesis in Systems, Control and Mechatronics

LOWISA HANNING

Department of Electrical Engineering
CHALMERS UNIVERSITY OF TECHNOLOGY
Gothenburg, Sweden 2018

Master's thesis 2018:027

Pulse Shaping of Radar Transmitters

Compensation of Memory Effects through Digital Pre-distortion

LOWISA HANNING

Department of Electrical Engineering
Systems and Control
Chalmers University of Technology
Gothenburg, Sweden 2018

Pulse Shaping of Radar Transmitters
Compensation of Memory Effects through Digital Pre-distortion
LOWISA HANNING

Manager: Fredrik Ingvarson, Saab AB
Supervisor: Mattias Thorsell, Saab AB
Examiner: Jonas Sjöberg, Department of Electrical Engineering

Master's Thesis 2018:027
Department of Electrical Engineering
Systems and Control
Chalmers University of Technology
SE-412 96 Gothenburg
Telephone +46 31 772 1000

Typeset in LaTeX
Printed by [Name of printing company]
Gothenburg, Sweden 2018

RF Pulse Shaping of Radar Transmitters
Compensation of Memory Effects through Digital Pre-distortion
LOWISA HANNING
Department of Electrical Engineering
Chalmers University of Technology

Abstract

The introduction of gallium nitride (GaN) power amplifiers (PAs) in the transmitter chain of pulsed radar architectures has proved to be advantageous compared to the previously used gallium arsenide (GaAs) PAs. However, it has also introduced new challenges in the system design due to thermal and electrical memory effects which leads to transients in the amplitude of the PA output.

It is therefore of interest to pre-compensate for the memory effects such that a desired shape of the pulse is maintained. This thesis evaluates the possibilities to use an iterative learning control scheme (ILC) to improve the shape of the pulse. The research is built upon measurements the PA output, where the PA is turned on and off in between the RF pulses. Two different pulse widths (PW) are evaluated, 10 μs and 100 μs. Black box modelling are performed to be able to test the algorithm offline, but also to understand the behaviour of the transients. Thereafter the ILC algorithm is implemented both in simulation and experiments.

Measurements showed that there were mainly two behaviours to compensate for in the PA output, first one oscillating transient and thereafter a decaying behaviour. Black box modelling showed that different model structures were needed for pulses of different duration. When implementing the ILC algorithm, it was possible to fully compensate for all undesired effects in simulation. In experiments the oscillating transient was not possible to fully compensate for whereas the decaying behaviour was eliminated.

Keywords: digital pre-distortion, PA modelling, pulse shaping, radar transmitters, memory effects, system identification, iterative learning control, Gallium Nitride.

Acknowledgements

I would like to thank my manager at Saab AB Fredrik Ingvarson who gave me the opportunity to work with my thesis in his group. Thanks to my supervisor Mattias Thorsell who came up with the idea of this thesis and always gave me support throughout the project. Special thanks to my examiner Jonas Sjöberg at the department of Electical Engineering who always been open to discuss my work, which especially has been helpful in the System identification and black box modelling. I would also like to thank Thomas Eriksson at the department of Electrical Engineering who has given me great support related to modelling of PAs and pre-distortion techniques. I would like to thank the people at the Microwave Electronics Laboratory at Chalmers who have guided me in the lab. Special thanks to Johan Bremer who has supported me with practical issues related to the measurements. Lastly I would like to thank my opponents Fredrika Zeidler and Marius Grimstad for giving me feedback on the report.

Lowisa Hanning, Gothenburg, June 2018

Contents

Acronyms

ADC	Analogue to Digital Converter
ARMAX	AutoRegressive Moving Average with eXogenous input
ARX	AutoRegressive with eXogenous input
CPI	Coherent Processing Interval
DAC	Digital to Analogue Converter
DPD	Digital Pre-Distortion
DUT	Device Under Test
FIR	Finite Impulse Response
GaAs	Gallium Arsenide
GaN	Gallium Nitride
ILA	Indirect Learning Architechture
ILC	Iterative Learning Control
IQ	Inphase and Quadrature
LNA	Low Noise Amplifier
MILA	Model-based Indirect Learning Architechture
MSE	Mean Squared Error
NRMSE	Normalized Root Mean Squared Error
OE	Output Error
PA	Power Amplifier
PRI	Pulse Repetition Interval
PW	Pulse Width
RF	Radio Frequency
VSA	Vector Signal Analyzer
VSG	Vector Signal Generator

List of Figures

List of Tables

1

Introduction

This chapter will give a background to why pulse shaping techniques for radar transmitters are relevant and a short review of the concept will be given. The chapter also serves a short review of previous research within the area. This is followed by a summary of the contribution of this thesis and the most important results are reviewed.

1.1 Background

Many radar systems that need to determine both position and speed use pulse timing techniques, where the time elapsed to receive an echo is used to determine the distance to an object and the Doppler effect of the returned signal is used to determine its velocity [1]. The shape of the transmitted pulse is relevant for both the performance of the radar, as well as it directly determines the frequency spectrum of the signal. In terms of radar performance, the range which the radar system is able to see depends on several parameters, but for instance the power of the transmitted pulse [2]. Other important characteristics are the pulse repetition frequency, duty cycle and pulse width (PW).

A power amplifier (PA) is used in the transmitter chain to amplify the signal to a level suitable for transmission. The introduction of gallium nitride (GaN) PAs has proven to be advantageous compared to the previously gallium arsenide (GaAs) PAs. Higher output power, higher efficiency and the ability to operate at higher temperatures [3], [4] are some of the beneficial characteristics just to mention a few. Implementation of GaN PAs has shown, despite its promising properties, that new challenges also are introduced [5]. One challenge is memory effects which leads to transients in amplitude and phase of the PA output, both in one single pulse but also from pulse-to-pulse [6], meaning that the output amplitude and/or phase differs from one pulse to another. This is a result of for instance temperature changes due to self heating of the device [7], [8]. Other sources to memory effects that have been discussed are the biasing network which actuates the system [9] and electron traps which leads to a decrease in maximum current and lower maximum output power and efficiency [10].

For the processing in pulsed radar, the pulse-to-pulse stability is of certain interest. Specifically it is of interest that each pulse within a coherent processing interval (CPI) has the same characteristics [1]. The introduction of memory effects might therefore influence the radar performance negatively, and it is of interest to pre-compensate for the memory effects such that each pulse within a CPI achieves the same amplitude. The use of pre-compensation techniques are usually referred to as digital pre-distortion (DPD) and the concept is to introduce a block in the chain which contains the inverse behaviour of the PA. Thereby, the desired shape of the output signal can be fed to the DPD, which outputs a predistorted signal which is used as input to the PA. This concept is illustrated in Figure 1.1. The initial PA output is shown in Figure 1.1a, where a transient in the PA output is present. In Figure 1.1b the DPD has been implemented and a predistorted input signal is sent to the PA, which in turn gives a desired shape of the PA output.

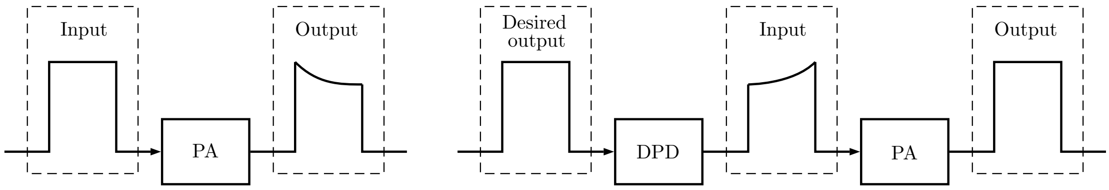

(a) PA response **(b)** PA response with DPD

Figure 1.1: The idea of using pulse shaping techniques to pre-compensate for undesired memory effects.

DPD techniques are commonly used within communication systems, but in such applications the main focus is to reduce spectral regrowth due to the strict requirements for the allowed spectral leakage into neighbouring channels [11]. Such applications therefore often aims at compensating for the nonlinear distortion. In [12], an iterative learning control (ILC) scheme was presented, which is an iterative process to find the optimal input signal that drives the system to a desired output response. One disadvantage discussed is that the algorithm requires that the same desired output response must be used for each iteration. In communication systems, where the signals are constantly changing, this is not suitable and the algorithm is proposed to be used to gain knowledge of the optimal input signal. Thereafter that knowledge can be used to design more advanced algorithms. For radar systems, where the desired output signal is pre-defined and not constantly changing, the algorithm can be used to find an input signal which compensates for the introduced memory effects. Implementation of more advanced algorithms are thereby not needed.

Another pre-compensation technique is presented in [13], where the DPD algorithm compensates for memory effects in pulsed radar systems. A GaN PA was biased with constant gate- and drain voltage and the system was thereafter excited with a train of RF pulses. The proposed DPD technique successfully compensates for differences in average amplifier gain for individual pulses within a CPI. One disadvantage with using constant gate- and drain voltage is that it further increases self heating and in order to avoid this phenomena, the PA should be turned off in between the RF pulses.

1.2 Thesis contribution

In this thesis, an evaluation of using DPD techniques to pre-compensate for memory effects such as self heating and transients from the biasing network is presented. In contrast to the study presented in [13], this research uses pulsed biasing which means that the transmitting PA is turned off between the pulses. This reduces self heating since the thermal dissipation is reduced when the PA is off. Another difference is that the goal in this research is to achieve a desired shape for a single pulse whereas the DPD in [13] compensates such that the same average gain for pulses within one CPI is achieved.

This research is built upon measurements of the PA output, where pulses with PW 10 μs and 100 μs each have been measured. Black box modelling of the relationship between the PA input and output has been performed for two main purposes. The first purpose is to be able to test DPD algorithms offline and get an estimate of how the shape of a pulse can be improved. The second purpose is to achieve a deeper understanding for the behaviour of the memory effects, and what model structure that is needed for pulses of different duration. With a suitable model, the ILC algorithm from [12] is implemented first in simulation and thereafter in experiments.

Results from measurements show that there are two characteristic behaviours that is of interest to compensate for in the PA output. First there is an oscillating behaviour and thereafter a decaying behaviour leading to a reduced transmitted power. In the black box modelling it could be concluded that a finite impulse response (FIR) model is sufficient for the testing DPD algorithms. Other model structures were however also studied and it showed that a nonlinear Wiener model is needed to achieve good simulations for a 100 μs pulse whereas for the 10 μs pulse a linear output error (OE) model is sufficient. The implementation of the ILC algorithm in simulation successfully eliminated the memory effects and a desired pulse shape could be achieved. In experiments it was possible to compensate for the decaying behaviour but the initial oscillations remained, which were due to problems with unknown delays and timing of instruments in the laboratory.

1.3 Thesis outline

The chapters in this thesis will be organized as follows. Chapter 2 serves an introduction to the system under investigation, namely the pulsed radar system. Further, this thesis focuses on the transmitter, and therefore a review of the transmitter chain is given. Chapter 3 presents the measurements used to capture memory effects. The measurement setup is explained and some challenges, such as synchronization of instruments and time alignment of data, are reviewed. Chapter 4 presents the black box modelling of the input-output relationship of the PA. Thereafter, in Chapter 5, the ILC scheme is explained and implemented both in simulation and experiments. Chapter 6 concludes the thesis by giving a summary of the results and in the last chapter future research questions are proposed.

2

System description

This chapter gives a brief review of the pulsed radar system and its transmitter chain. Some microwave components and characteristics for a pulsed radar signal are introduced. Mathematical description for the radar signal are also given, both for the radio frequency (RF) signal and its baseband equivivalent representation.

2.1 Pulsed radar

A simplified block diagram of a radar system is depicted in Figure 2.1. An analogue baseband signal x is generated by the digital-to-analogue converter (DAC). The signal is thereafter up-converted to carrier frequency by a mixer which multiplies the baseband signal with a sinusoidal signal generated by a local oscillator. The RF signal $\tilde{x}$ is amplified by the PA to a level suitable for transmission, where the amplified RF signal is denoted $\tilde{y}$. After the amplification the antenna allows the signal to propagate in space and if a target is present the antenna receives energy of a returned echo. The signal received is often weak, and is therefore amplified before any processing or decisions regarding detection. Since the detection is noise sensitive, this amplification is done by a low noise amplifier (LNA) which operation adds little noise. Before any processing and decisions whether a target is present, down-conversion back to digital baseband form is done. The mixer and the local oscillator converts the signal $\tilde{z}$ back to analogue baseband z and the analogue-to-digital converter (ADC) converts the baseband signal to digital domain. [2]

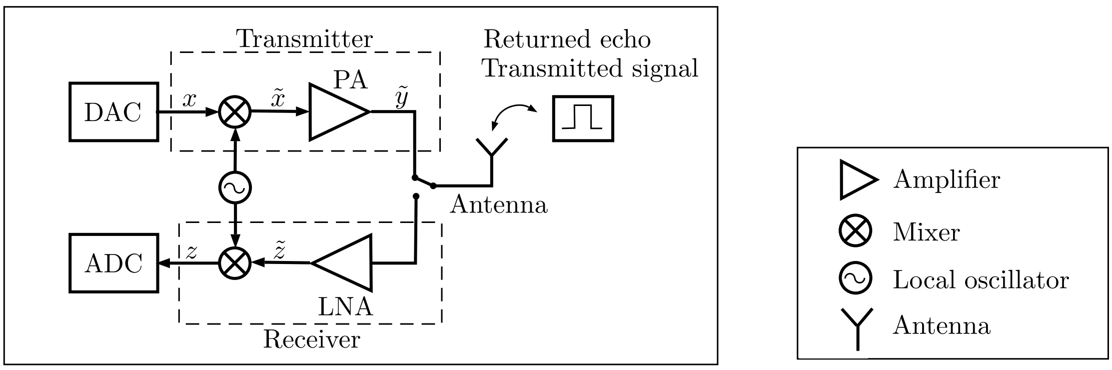

Figure 2.1: Block diagram of a pulsed radar architecture and explanation of symbols corresponding to common microwave components.

An increased transmitted power implies longer detection range, but it might also cause nonlinear distortion depending on the maximum output power of the PA, which in turn leads to deterioration of the signal and spectral regrowth. Using high power for the transmitted signal also requires that it is possible to isolate the receiver, this is usually done by switches [1]. When the system switches to receiving mode the transmitting PA should be turned off in order to save energy and prevent heating. According to the radar range equation, the maximum range R_{max} will be proportional to the fourth root of the transmitted peak power P_{pk}, given by

$$R_{max} \propto \sqrt[4]{P_{pk}}.$$

Therefore, it is desired to have a high peak power of the transmitted pulse. It is however noteworthy that in order to double the maximum range the transmitted peak power must be increased with a factor 16.

2.2 The transmitter chain

It is known that RF transmitters suffer from memory effects and also nonlinear distortion. All hardware parts in its chain have imperfections which affects the transmitted signal. Memory effects such as self heating occurs due to heat dissipation [14], and the main source is the PA due to its high power operation. For modelling of memory effects and nonlinear distortion, often a baseband version of the transmitter chain is used. This is possible since the envelope of the transmitted signal contains all useful information and the up-conversion is performed to allow the signal to be transmitted [15]. The whole transmitter chain and its equivivalent baseband representation are depicted as block diagrams in Figure 2.2. The pulses into the PA represents that the PA is turned on/off in between the RF pulses.

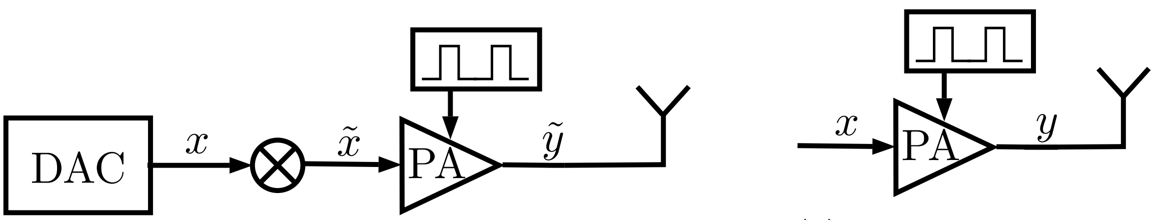

(a) Pulsed radar transmitter chain.

(b) Baseband equivivalent transmitter chain.

Figure 2.2: Transmitter chain and its equivalent form commonly used for modelling of memory effects and nonlinear distortion. For the whole chain, the baseband signal x is up-converted to its the carrier waveform $\tilde{x}$ where its amplified by a PA. Its equivivalent baseband form neglects the up-conversion.

A time domain representation of a radar pulse is shown in Figure 2.3. The figure shows the envelope and the upconverted RF pulse. The figure also denotes the on/off periods for the transmitter and the receiver, where $T_x = 1$ and $T_x = 0$ means that the transmitter is on and off respectively. The same logic holds for the receiver, R_x, and as can be seen the receiver is off when the transmitter is on and vice versa. The pulse repetition interval (PRI) is shown, which is the time elapsed from one pulse to another. Another pulse characteristic is pulse width (PW), denoted τ. A CPI consists of a set of pulses with the same characteristics.

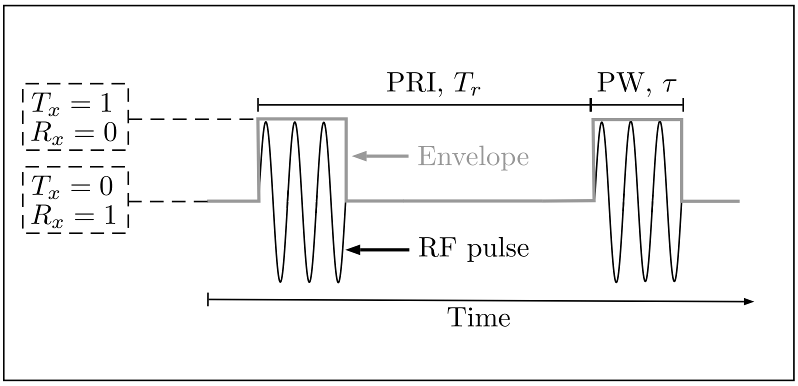

Figure 2.3: Radar pulse in time domain.

The upconverted RF signal can be described using the following identity

$$\tilde{x}(t) = A(t)\cos(\omega_c t + \theta(t)), \tag{2.1}$$

where ω_c is the angular carrier frequency and $A(t)$ is an amplitude modulation and $\theta(t)$ is a phase modulation of the RF signal [15]. Using trigonometric identities on (2.1) the following description is achieved

$$\tilde{x}(t) = \underbrace{A(t)\cos(\theta(t))}_{I(t)}\cos(\omega_c t) - \underbrace{A(t)\sin(\theta(t))}_{Q(t)}\sin(\omega_c t), \tag{2.2}$$

where $I(t)$ and $Q(t)$ is called the in-phase and quadrature (IQ) components respectively. Further, (2.1) can be written in complex form according to

$$\tilde{x}(t) = \Re\{A(t)e^{j\omega_c t}e^{j\theta(t)}\} = \Re\{x(t)e^{j\omega_c t}\}. \tag{2.3}$$

In (2.3), $x(t)$ is the baseband signal, often called complex envelope. As mentioned, the baseband signal contains all useful information whereas the RF signal allows it to be transmitted. The baseband signal is often written in terms of the inphase and quadrature components, according to

$$x(t) = I(t) + jQ(t). \tag{2.4}$$

In DPD the aim is thereby to pre-compensate for memory effects such that a desired shape of the envelope of the signal at the PA output y is achieved. This signal will thereafter be the signal that propagates in space and hence it determines the radar performance.

3

Measurements

This chapter presents the measurements that have been performed to capture the memory effects that are of interest to compensate for. First the setup and its synchronization are presented, thereafter the initial experiments that were performed to be able to model the system are shown.

3.1 Measurement setup

The device under test (DUT) is the transmitter GaN PA on a transceiver. A Rohde & Schwarz SMU200A vector signal generator (VSG) is used to generate the baseband input signal. It has a frequency range from 100 kHz to 6 GHz and can be remotely controlled through MATLAB and SCPI[1] commands. It is also possible to generate an arbitrary digital baseband IQ signal and upload it to the VSG which thereafter converts the signal to analogue domain and up-converts it to carrier frequency. The output signal from the DUT is measured by an Agilent N9030A PXA vector signal analyzer (VSA). The VSA has a frequency range from 3 Hz to 50 GHz and is also possible to remotely control through MATLAB and SCPI commands. The DUT uses a DAC with on/off control for the bias supply in order to turn the PA on and off in between the RF pulses. Communication with the DAC is done with I^2C protocol and a programming card are used to perform this. Thereby, both the DAC and the DUT needs several power supplies. The DAC also needs a pulse generator to switch between on and off mode. A simplified block diagram of the setup are depicted in Figure 3.1 and the equipment are shown in Figure 3.2.

In order for the experiments to be repetitive, the instruments needs to be synchronized. When a new period of the input signal is started, a trigger is sent to the pulse generator which allows the pulse generator to set $T_x = 1$ and its bias supply is activated. Another trigger is sent to the VSA which starts to measure the PA output signal. The trigger signal is however not instantaneous and there occurs a delay both until the the VSA starts to measure the signal and until the PA is turned on.

The VSG, the VSA and the bias pulses are assumed to be ideal which implies that all deterioration of the signal arises from imperfections in the PA. I.e. the assumptions made are that a perfect bias pulse is generated by the DAC and that the mixer that upconverts the signal to RF is ideal. This is motivated by the fact that the PA is the main cause for the memory effects, and even if other components in its chain also affects, the main contribution will be from the PA. This also enables

[1]SCPI = Standard Commands for Programmable Instruments

the possibility to use the baseband equivivalent representation of the transmitter chain in the modelling.

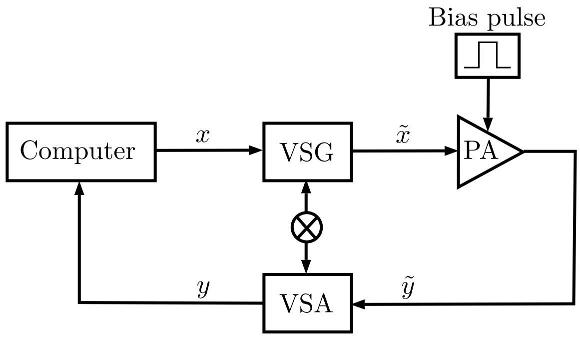

Figure 3.1: Block diagram of measurement setup. A computer generates the IQ-baseband input signal x which thereafter is upconverted to carrier frequency $\tilde{x}$ by a VSG. The signal is amplified by the PA and its RF output signal $\tilde{y}$ is measured and down-converted to baseband form y by a VSA. The PA is turned on and off by using pulsed bias.

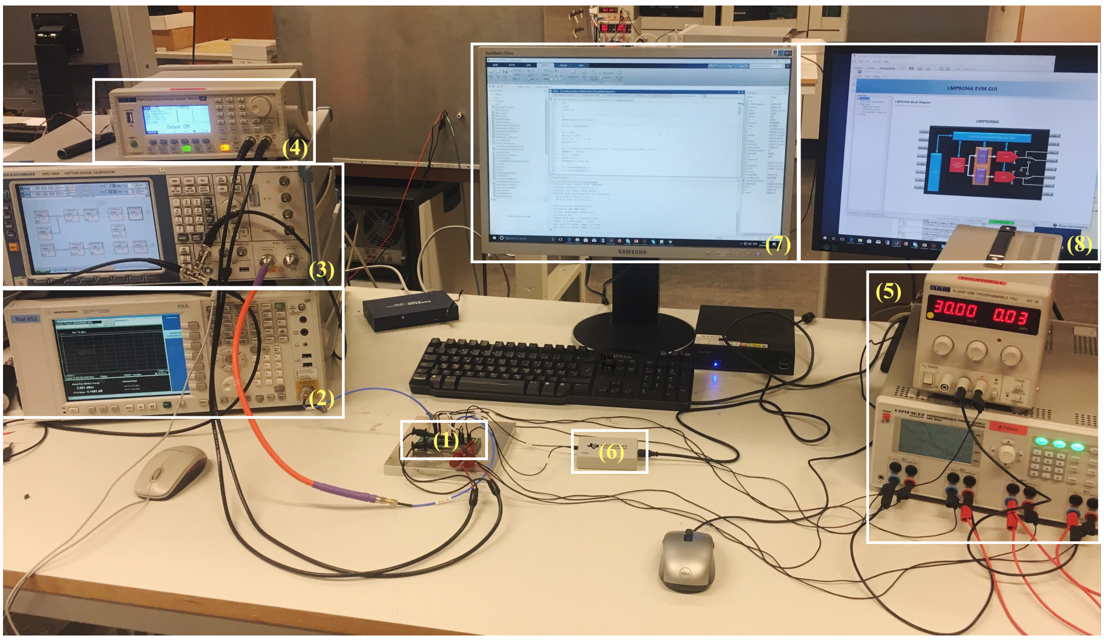

Figure 3.2: Measurement setup in laboratory, consisting of (1) DUT, (2) VSA, (3) VSG, (4) pulse generator, (5) power supplies, (6) programming card, (7) MATLAB to communicate with VSA and VSG and (8) GUI to communicate with the programming card.

3.2 Data collection

For the data collection, the baseband signal x was generated with a clock frequency of 100 MHz, which is the maximum clock frequency for the VSG. The sampling frequency for the VSA should be selected such that it is equal to or a multiple of the clock frequency for the VSG. The maximum sampling frequency was 175 MHz, and therefore it was selected to be equal to the clock frequency, i.e. 100 MHz. In order to reduce some complexity for the measurements, the baseband input signal was set to a constant value, and only the on/off control of the PA was used to achieve a pulsed input signal to the PA. Another possibility would be to use a pulsed baseband input signal and the on/off control, but this would require more knowledge about timing and synchronization of the system. The inphase component was set to 0.71 V for each time instance and the quadrature component was set to 0 V. Assuming a system with 50 Ω impedance, this leads to a power level of 7 dBm which allows the PA to operate in its linear regime. The carrier frequency was selected to 5.9 GHz. Two different pulse widths of the bias pulse have been evaluated, one with a 10 μs duration and one with a 100 μs duration. The input signals are depicted in Figure 3.3 below. Note that in the figure the bias pulses starts at τ instead of 0, this is to show that there is a short delay from when the trigger reaches the pulse generator and the PA is turned on.

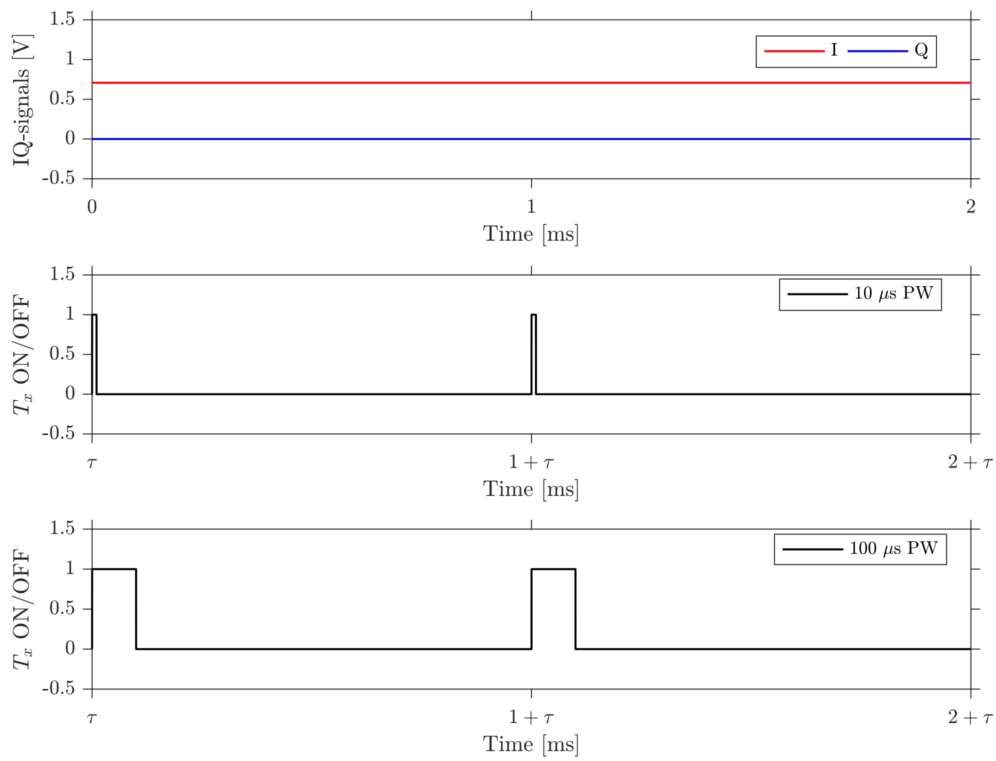

Figure 3.3: Input signals used for the data collection. Top figure shows the baseband signal x. As can be seen the baseband signal have been selected to constant values. In the middle figure the bias pulse with 10 μs pulse width are shown and the bottom figure shows the bias pulse with 100 μs pulse width. The VSG generates a sequence that is 1 ms long, and thereafter it repeats the same sequence. Every time a new period is started for the VSG a trigger is sent to the pulse generator which in turn generates the bias pulses.

When the input signals are programmed and uploaded to their respective instrument, the VSG starts to repetitively play the same sequence. As seen in Figure 3.3, the sequence is repeated after 1 ms and the PA is on for 10 μs or 100 μs, followed by a period when the PA is off and consequently there is no output from the PA. A command is sent to the VSA to start collect data, which then waits for a new trigger from the VSG. When the trigger is received, the VSA starts to measure the PA output baseband signal y for 1 ms which is the PRI. Figure 3.4 and 3.5 shows measurements of 100 pulses with PW 10 μs and PW 100 μs respectively, where a) shows the whole pulse, b) shows the response when the PA is turned on and c) shows some oscillations that were present in the output. As can be seen, there is a short initial delay until a step in the output occurs. The 100 measurements shows that the behavior is repetitive and will therefore also be predictive. One observation that can be made is that there are some problem with the timing since the rise of the pulse do not occur exactly at the same time, this can be seen in the bottom left figures b). Another observation that can be made is that the mean amplitude for the 100 μs pulse differs from the amplitude for the pulse with 10 μs PW. The reason is that the second pulse is kept on for a longer period, hence its heat dissipation is increased and it has less time to cool down in between the pulses.

In order to increase the comparability of the pulses, a time alignment of the data was performed. The data was upsampled such that more samples were generated and then the data was shifted such that the rise of each pulse occurred at the same sample. After the alignment, the data was downsampled back to the original sampling frequency. The time aligned pulses are shown in Figure 3.6 and 3.7.

For both the 10 μs pulse and the 100 μs it is clear that there are some undesired behaviour for the PA output. There are some initial oscillating transients that probably occur due to imperfections in the biasing network. It can also be observed that there are a decaying behaviour due to heating which is more obvious for the pulse with longer duration.

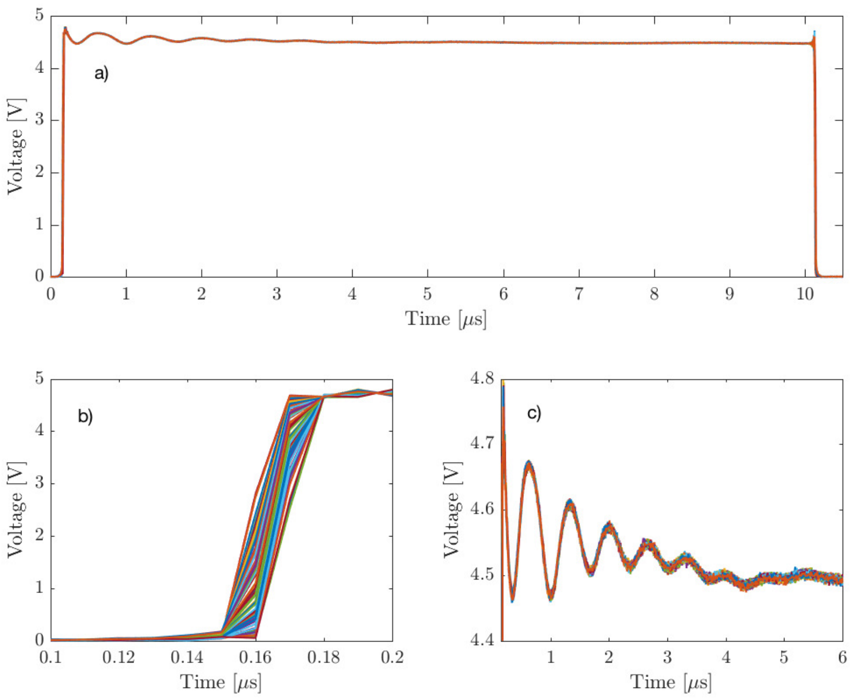

Figure 3.4: Measurements of 100 pulses with 10 μs pulse width. The figures have different ranges for the time axis, where a) shows whole pulse, b) shows the output response when the PA is turned on and c) the oscillating transients.

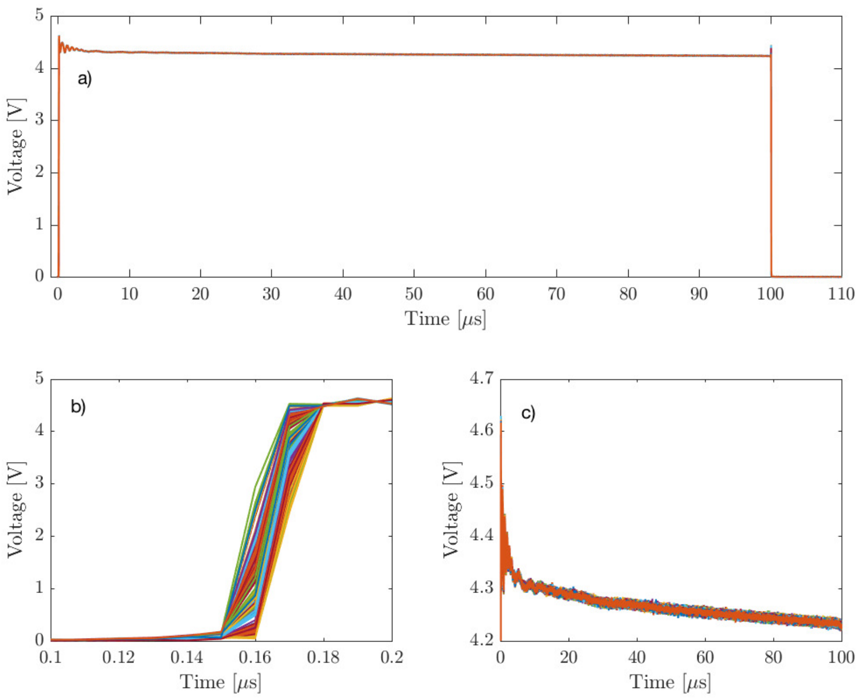

Figure 3.5: Measurements of 100 pulses with 100 μs pulse width. The figures have different ranges for the time axis, where a) shows whole pulse, b) shows the output response when the PA is turned on and c) the oscillating transients.

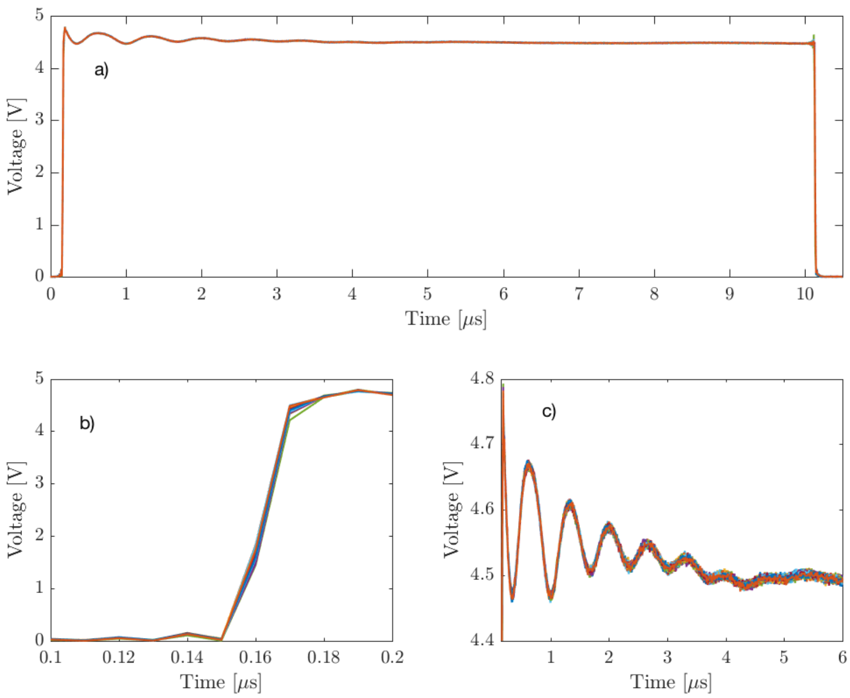

Figure 3.6: Time aligned data of 100 pulses with 10 μs pulse width. The figures have different ranges for the time axis, where a) shows whole pulse, b) shows the output response when the PA is turned on and c) the oscillating transients.

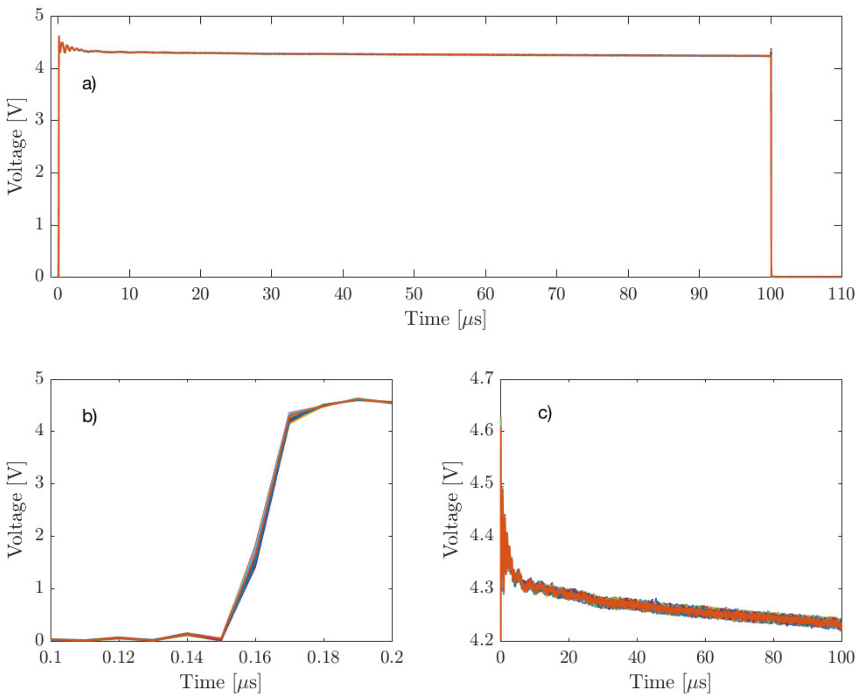

Figure 3.7: Time aligned data of 100 pulses with 100 μs pulse width. The figures have different ranges for the time axis, where a) shows whole pulse, b) shows the output response when the PA is turned on and c) the oscillating transients.

4

Power amplifier modelling

This chapter presents the modeling approach used to describe the input-output relationship for the measurements presented in Chapter 3. First the aim with the modelling is presented, followed by a presentation of the input and output signals that have been used. Thereafter some commonly used model structures and the methodologies used to estimate their parameters will be reviewed. Performance evaluation of the models are introduced which is followed by a presentation of some estimated models.

4.1 Modelling aim

There are mainly two purposes with the modelling. Firstly, a model is needed to test and evaluate DPD algorithms. This will enable the possibility to simulate the system such that a new input signals can be tested and its response can be evaluated before applying it in experiments. Secondly, a deeper understanding for the dynamics of the system is also desired. The model should describe the relationship between the measured baseband output signal y and the baseband input signal x, i.e. $y = f(x)$. Black box models and system identification are used, where a set of input-output measurements are used to characterize their relationship, hence no internal structure or physical parameters of the system are taken into consideration [16]. Some model structures might be good for making predictions, where measurements are utilized to predict how the system will behave k-steps ahead. In this case no new measurements will be available, and instead a model performing good in simulation is needed.

4.2 Input and output signals

The models will later be used to test DPD algorithms on, where the purpose is to compensate for effects when the PA is on, thus a model performing well during that period is desired. It is thereby not necessary to model the period when the PA is off and it is sufficient to instead model a step and cut the data from where the PA is turned off. Using the step response also enables the possibility to directly estimate the impulse response through differentiation.

The baseband input signal x has in the modelling part been considered to be 0 when the amplifier is off, and A for the period when its on, where A is its voltage level which depends on the selected power level. The power level of the input signal was set to 7 dBm in the measurements which gave a voltage level of $A = 0.71$ V for a source impedance of 50 Ω. As shown in the previous chapter, the baseband signal was set to a constant in the measurement, however when the PA is off no input is present and hence it must be 0 in the modelling. The signals that have been considered as input and output are shown in Figure 4.1a and 4.1b.

Estimating models from one single measurement proved to be challenging due to sensitivity to noise. Hence, a mean value from all 100 measurements has been used to estimate all models except from the finite impulse response (FIR) where another approach has been used. This results in less noise in the output which can be motivated using the block diagram in Figure 4.2. The block diagram consists of a transfer function G, an input x, process noise e_1, measurement noise e_2 and the measured output y. The process noise and the measurement noise is stochastic and therefore their contribution to the measured output will be at different frequencies for each measurement. Provided that the same input signal x is used for each measurement, one will get more information at the distinct frequencies which the true plant output consists of, whereas the noise will contribute with components at different frequencies.

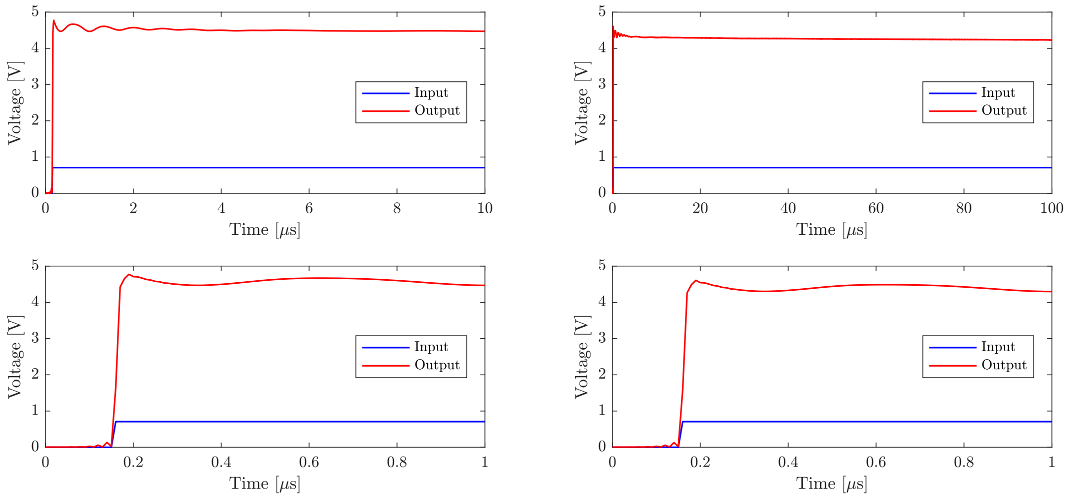

(a) 10 μs pulse **(b)** 100 μs pulse

Figure 4.1: Input and output signals that have been used in the modelling.

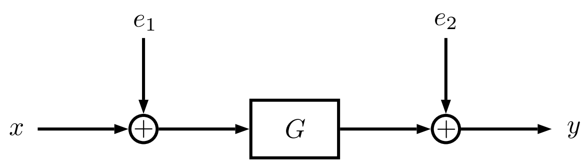

Figure 4.2: Block diagram illustrating the plant, with input x, process noise e_1, measurement noise e_2 and measured output y.

4.3 Model structures

This section will give a brief review of some standard models used for black box modelling. The models will in this thesis be used to simulate the PA output with new input signals.

One model taken into consideration is the finite impulse response (FIR). The output signal is then represented as a sum of current and previous input signals times their corresponding coefficients, according to

$$y(n) = \sum_{i=0}^{n_h-1} h_i x(n-i). \tag{4.1}$$

The FIR filter (4.1) includes no feedback since there is no terms including previous values of the output. It is thereby an all zero model and the filters are unconditionally stable. [17]

Another class of models, which incorporates both poles and zeros, are time series models where the ARMAX[1] is one important family of model structures [18]. An ARMAX model have the following structure

$$A(q)y(n) = q^{-d}B(q)x(n) + C(q)e(n). \tag{4.2}$$

where A, B, C are polynomials according to

$$A(q) = 1 + a_1q^{-1} + \ldots + a_{n_a}q^{-n_a}, \tag{4.3}$$

$$B(q) = b_0 + b_1q^{-1} + \ldots + b_{n_b}q^{-n_b}, \tag{4.4}$$

$$C(q) = 1 + c_1q^{-1} + \ldots + c_{n_c}q^{-n_c}, \tag{4.5}$$

d is an input time delay, $e(n)$ is a white noise stochastic process and q is the time shift operator[2]. The goal is then to estimate the unknown parameters $\boldsymbol{a}$, $\boldsymbol{b}$ and $\boldsymbol{c}$.

One important special case of the ARMAX model structure is the ARX[3] model, written

$$A(q)y(n) = q^{-d}B(q)x(n) + e(n). \tag{4.6}$$

This structure enables the possibility to reformulate the model such that linear regression can be utilized to estimate the parameters.

For simulations the OE model has proven to be advantageous since it is a pure simulation model and cannot be used for predictions. The model structure is written as

$$y(n) = \frac{q^{-d}B(q)}{F(q)}x(n) + e(n), \tag{4.7}$$

with $F(q) = 1 + f_1q^{-1} + \ldots + f_{n_f}q^{-n_f}$. An extension of the OE model is the Wiener-Hammerstein class where the linear transfer function extended with an input nonlinearity and/or an output nonlinearity. For a Wiener model a linear transfer function of OE type is connected to a static output nonlinearity, according to Figure 4.3a. The Hammerstein model consists of a static input nonlinearity followed by a linear transfer function of OE type, Figure 4.3b. Another possibility is a combination of the two models with both input and output nonlinearities resulting in a Wiener-Hammerstein model. [18]

[1] ARMAX = AutoRegressive Moving Average with eXogenous input

[2] $q^{-1}u(n) = u(n-1)$

[3] ARX = AutoRegressive with exogenous input

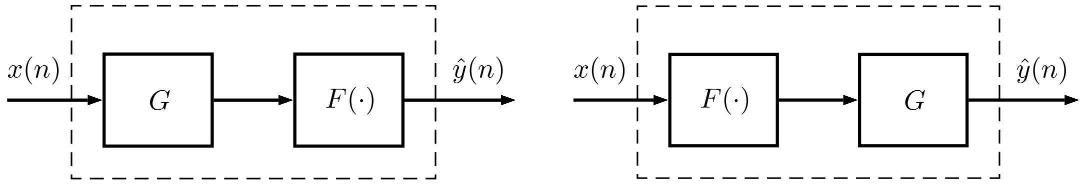

(a) Wiener model **(b)** Hammerstein model

Figure 4.3: Block diagrams of models with a linear transfer function G combined with a static nonlinearity $F(\cdot)$.

All model structures except the Wiener-Hammerstin can then be written as

$$y(n) = G(q)x(n) + H(q)e(n), \tag{4.8}$$

where $G(q)$ explains that plant behaviour and $H(q)$ determines how the process noise enters the system.

4.4 Parameter estimation

The goal is to minimize the residuals ε, i.e. the distance between the measurement and its estimate, given by

$$J(\theta) = \frac{1}{2}\sum_{n=1}^{N-1} \varepsilon^2(n) = \frac{1}{2}\sum_{n=1}^{N-1}(y(n) - \hat{y}(n))^2, \tag{4.9}$$

where $y(n)$ is the measured output and $\hat{y}$ is its estimate. For model structures that are not linear in its parameters, the estimation of the model coefficients is an iterative search for coefficients that minimizes the criterion given in (4.9). For model structures that are linear in its parameters (FIR and ARX) the linear least squares method can be utilized to estimate the parameters. The model estimated from a data set of N samples can then be written in a regressor φ which includes known signals times an unknown parameter vector θ with a white noise sequence $e(n)$ added.

$$y(n) = \varphi^T(n)\theta + e(n) \qquad n = 1, ..., N \tag{4.10}$$

Often (4.10) is written in vectors, according to

$$\underbrace{\begin{bmatrix} y(1) \\ \vdots \\ y(N) \end{bmatrix}}_{Y} = \underbrace{\begin{bmatrix} \varphi^T(1) \\ \vdots \\ \varphi^T(N) \end{bmatrix}}_{\Phi} \theta + \underbrace{\begin{bmatrix} e(1) \\ \vdots \\ e(N) \end{bmatrix}}_{E}. \tag{4.11}$$

Provided that $e(n)$ is zero in mean, the best guess one can make for one sample is to remove the noise, which gives the estimate $\hat{Y} = \Phi\theta$, and 4.9 can then be written as

$$J(\theta) = \frac{1}{2}(Y - \Phi\theta)^T(Y - \Phi\theta). \tag{4.12}$$

The linear least squares solution for the coefficients $\hat{\theta}_{LS}$, is then found setting the derivative of (4.12) equal to zero, which gives the solution

$$\hat{\theta}_{LS} = (\Phi^T \Phi)^{-1} \Phi^T Y, \tag{4.13}$$

where $(.)^T$ denotes the transpose and $(.)^{-1}$ is the matrix inverse. In the ideal case this would give the residuals ε to be equal to the white noise sequence e.

For the FIR model another approach can also be used to estimate the parameters. When the data is cut such that a step response is considered instead of a pulse response, the impulse response can easily be estimated by taking the first difference of the data. This operation to find the impulse response coefficients can be written as

$$h(i) = y(i) - y(i-1), \tag{4.14}$$

where $h(i)$ denotes the impulse response coefficient at index i. The impulse response will get a high number of coefficients, since the difference operation will give $N-1$ coefficients for a data set of N points. By estimating the impulse response from one measurement, a noisy estimate is achieved. Therefore, coefficients for all 100 measurements are derived, resulting in total $100 \times (N-1)$ coefficients. Thereafter, the impulse response model are found by taking the mean value for each coefficient.

4.5 Performance evaluation

When a model structure has been decided, its performance are evaluated by comparing its simulated response with the measured response. In the decision of a model structure, both its performance in terms of deviation from the measured response and also the number of model coefficients should be taken into consideration. An increased number of model coefficients gives an increased complexity in its practical implementation. A block diagram illustrating the performance evaluation process is shown in Figure 4.4.

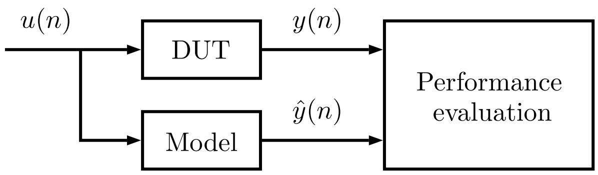

Figure 4.4: Block diagram describing how the performance evaluation for the black box models will be performed. The same input signal will be fed to the DUT and the model of the DUT. Thereafter their output responses will be compared and evaluated through different performance evaluation metrics.

The performance evaluation metrics considered are the mean squared error (MSE) and the normalized root mean squared error (NRMSE). These metrics evaluates how much the model in time domain deviates from its measurement. Using time domain metrics are motivated by the fact that the goal is to compensate for undesired effects in time domain, hence it is important to have a model which makes good estimates in time domain. How MSE and NRMSE are calculated are presented in Eq. 4.15

and 4.16 respectively. It is often desired to have the MSE as small as possible without overfitting the data. The NRMSE instead ranges between $[1, -\infty)$, where 1 implies perfect fit, 0 implies that the model fits the data no better than a straight line through the data.

$$\text{MSE} = \frac{1}{N}\sum_{n=1}^{N}(y(n) - \hat{y}(n))^2 \tag{4.15}$$

$$\text{NRMSE} = 1 - \frac{\sqrt{\sum_{n=1}^{N}(y(n) - \hat{y}(n))^2}}{\sqrt{\sum_{n=1}^{N}(y(n) - \bar{y})^2}} \tag{4.16}$$

In (4.16) $\bar{y}$ denotes the the mean value.

The data are divided into intervals that the performance are evaluated for. Observing the data, three different characteristic behaviours could be distinguished. First, there is a fast response when the step is applied. Thereafter, there is an oscillating behaviour and after approximately 5 μs the dominating oscillations have died out and there is instead a slowly decaying behaviour. The data are therefore divided into these intervals and also the whole sequence are evaluated. This is summarized in Table 4.1 and shown in Figure 4.5 for the 10 μs pulse. The 100 μs pulse are divided into similar intervals, also summarized in Table 4.1 and shown in Figure 4.6. It is for instance more important to have a good fit in interval (c) and (d) than interval (b). The initial fast response might be hard to compensate for in practice, and it is more important to compensate for the decaying behaviour in the end.

Table 4.1: Intervals that the data are divided into for performance evaluation of the models.

PW \ Interval	(a)	(b)	(c)	(d)
10 μs	0-9.99	0.1-0.65	0.65-5	5-9.99
100 μs	0-99.99	0.1-0.65	0.65-5	5-99.99

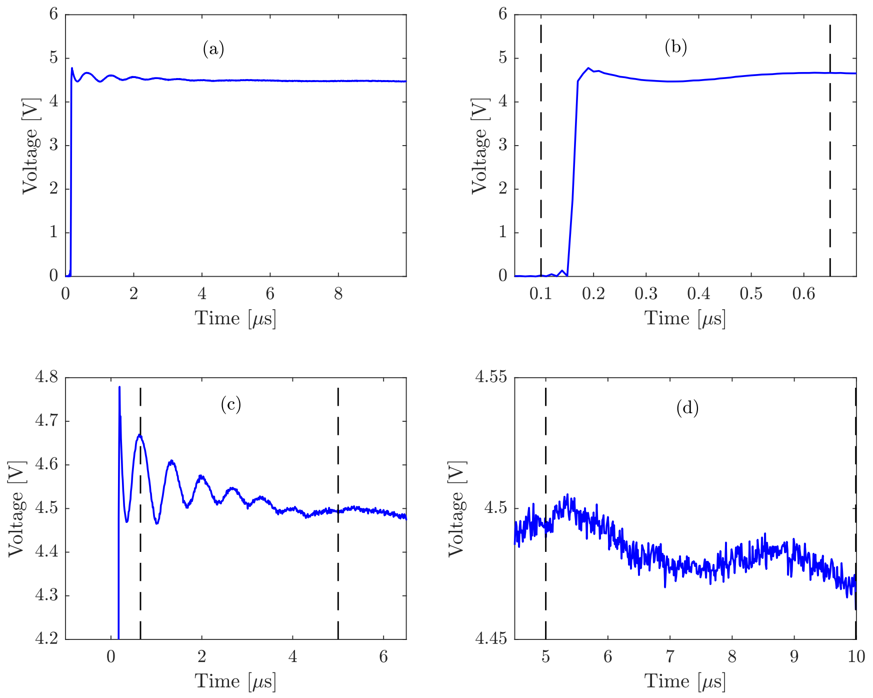

Figure 4.5: Intervals of the 10 μs pulse that the performance of the models will be evaluated for. The intervals in numbers are presented in Table 4.1.

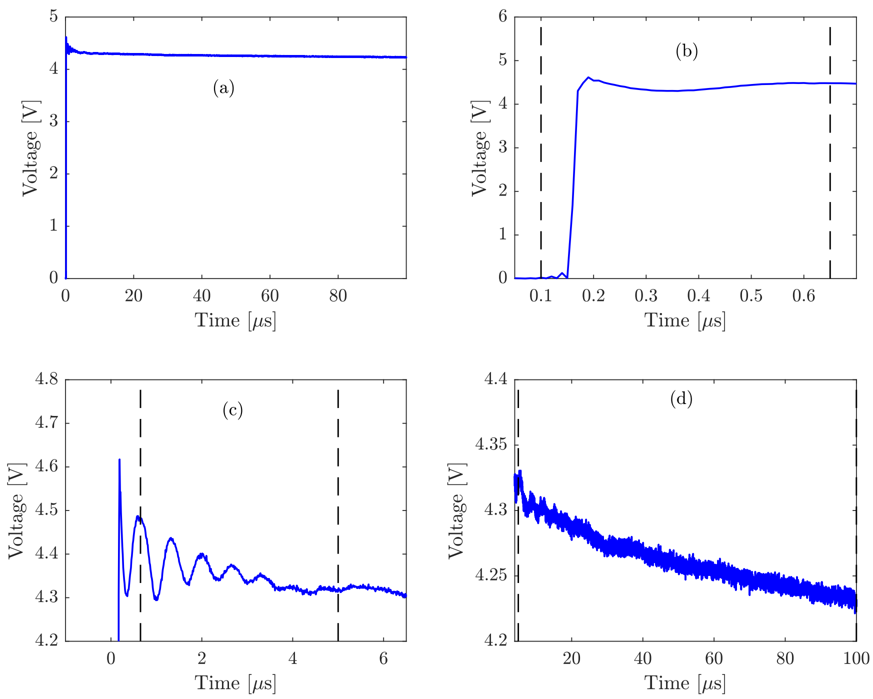

Figure 4.6: Intervals of the 100 μs pulse that the performance of the models will be evaluated for. The intervals in numbers are presented in Table 4.1.

4.6 Estimated models 10 μs pulse

Four models has been estimated for the 10 μs pulse, one FIR model, one OE model, one Wiener model and one ARX. The total number of coefficients for each linear transfer function are presented in Table 4.2. Note that the Wiener model also consists of a nonlinearity and some complexity is thereby added to the structure. In this case a sigmoidnet consisting of 10 units has been used as nonlinearity.

There is no input delay, as can be seen in the Figure 4.1a (lower), hence the delay d is 0 for all models. For the OE, 5 coefficients for the B polynomial are used, $n_b = 5$ and 4 coefficients for the F polynomial are used, $n_f = 4$. This model will be denoted OE/OE(5,4,0)[4]. The same structure for the linear transfer function in the Wiener model has been used. For the ARX, 6 coefficients have been used for the B polynomial, $n_b = 6$, and 5 coefficients for the A polynomial, $n_a = 5$. This model will be denoted ARX/ARX(5,6,0)[5].

This section will first present simulations of the estimated models, shown together with the mean value of the measurements. Simulations of each model presented together with all measurements can be found in Appendix A. The simulations are divided into the performance evaluation intervals presented in Table 4.1 and the performance evaluation metrics are shown as bar graphs. In the bar graphs, a mean value of each metric calculated from all 100 measurements are presented. Also some characteristics of each model are also presented, e.g. pole/zero maps, partial transfer functions and the nonlinearity of the Wiener model.

Table 4.2: Number of coefficients for linear transfer functions for the models estimated for the 10 μs pulse.

Coefficients \ Model	FIR	OE	Wiener	ARX
#	999	9	9	11

4.6.1 Simulations

Simulations of the whole step are shown in Figure 4.7 and the corresponding performance evaluation metrics are shown in Figure 4.8. As can be seen, all models except the ARX follows the oscillations (~0-4 μs). The MSE is significantly higher for the ARX than for the other models, Figure 4.8a. Despite this, all models achieves a high NRMSE, Figure 4.8b.

Figure 4.9 and Figure 4.10 shows simulations and metrics for interval (b). Also for this interval the performance of the ARX is worse than the other models. It can further be seen that the performance of the OE and the Wiener model is similar, whereas the FIR performs best both from the simulation and its performance metrics.

For the oscillations in interval (c), depicted in Figure 4.11 one can further see that the ARX does not achieve a desired behaviour. Again the FIR performs best,

[4] OE(n_b,n_f,d)
[5] ARX(n_a,n_b,d)

according to the metrics presented in 4.12 and the performance of the OE and the Wiener model are similar.

In Figure 4.13 the last part of the step is shown, namely interval (d). Here it can be seen that the mean value includes more noise than could be distinguished for the previous intervals. As can be seen, the FIR filter also follows the noise, which however less than the noise present in one single measurement. Even though the Wiener model achieves lower MSE and higher NRMSE than the OE model, one can see from the simulation that neither of the models follow the mean value of the measurements. Note however the range of the y-axis, which shows that the error in magnitude however is small.

To summarize, the FIR model performed the best in terms of lowest MSE and highest NRMSE for all intervals. An ARX model is not suitable for this application which can be explained by the fact that such model focuses on minimizing the one step prediction error and thereby is more suitable when it is desired to have a model that performs good in predictions. The OE and the Wiener model had similar performance, and hence it can be concluded that a linear OE model is sufficient and the nonlinearity is not needed.

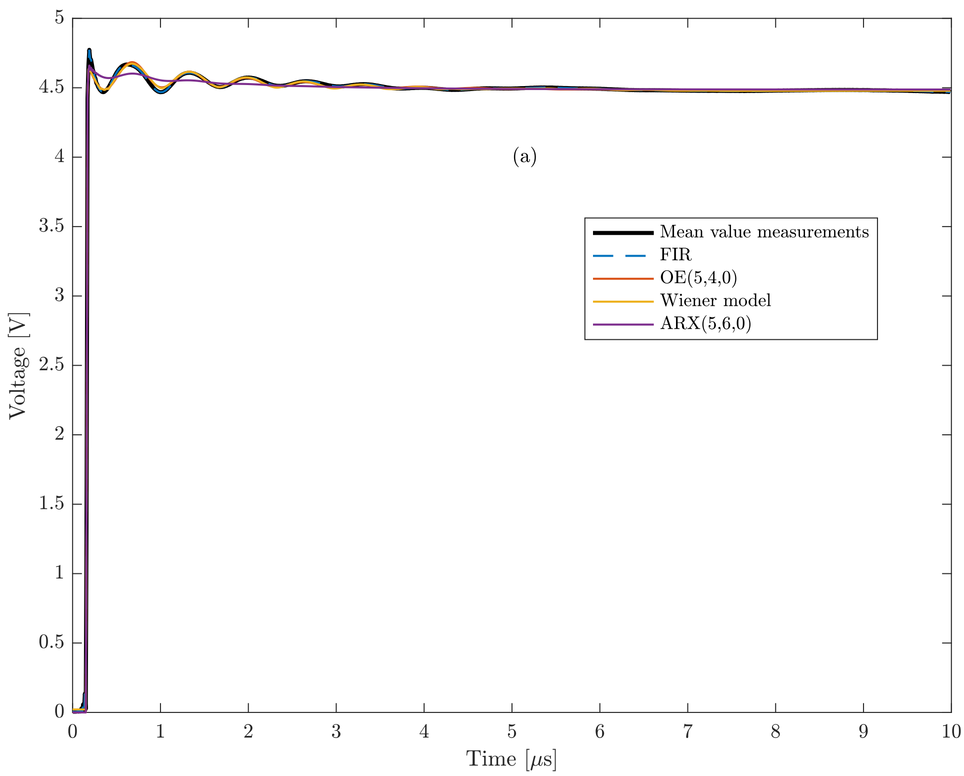

Figure 4.7: Simulated models together with mean value of the 100 measurements for the 10 μs pulse in interval (a).

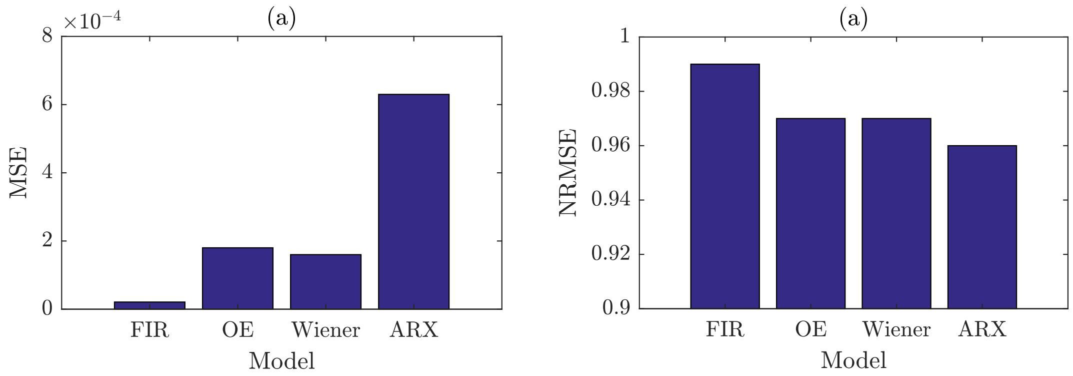

(a) MSE **(b)** NRMSE

Figure 4.8: Mean value of performance evaluation metrics calculated from all 100 measurements for the 10 μs pulse for interval (a).

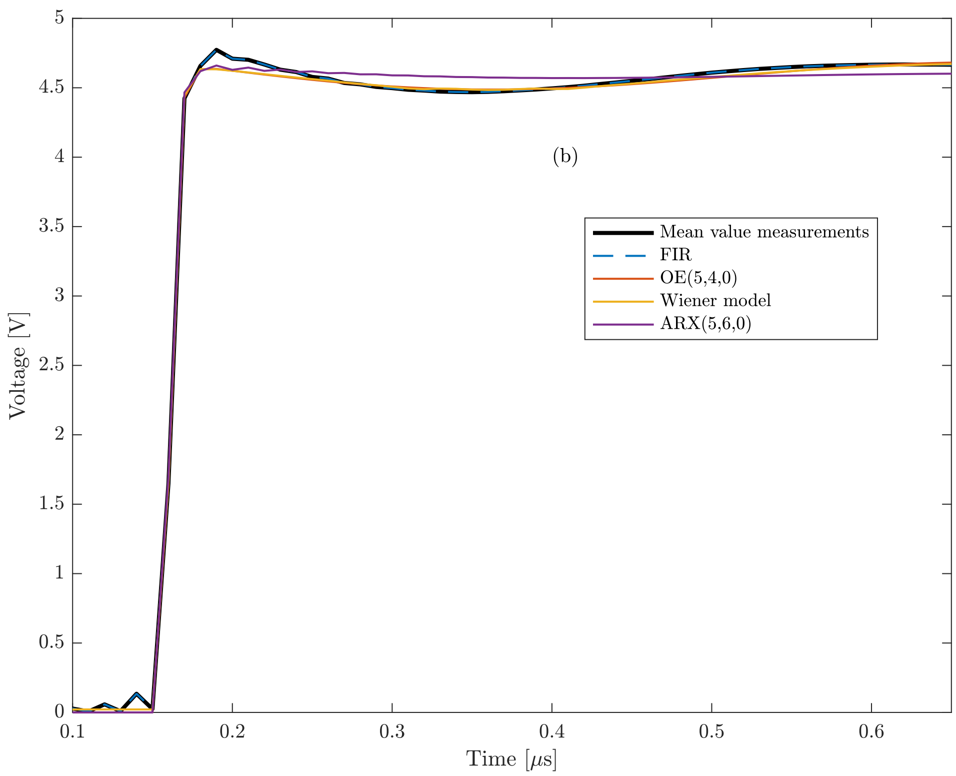

Figure 4.9: Simulated models together with mean value of the 100 measurements for the 10 μs pulse in interval (b).

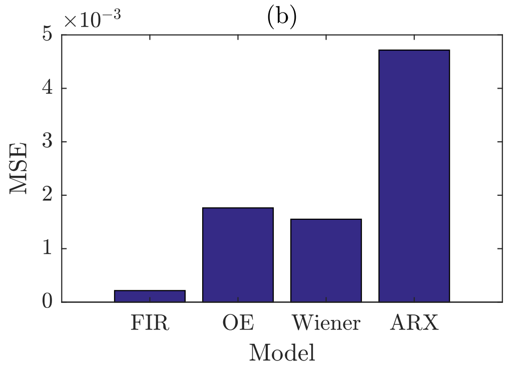

(a) MSE

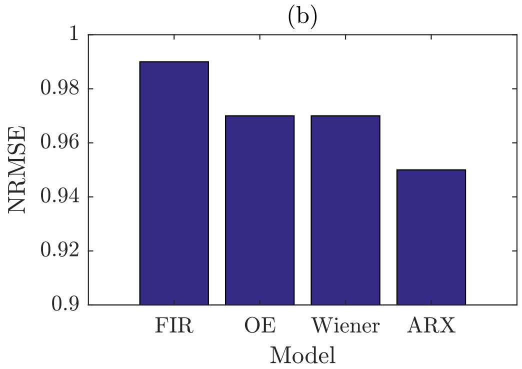

(b) NRMSE

Figure 4.10: Mean value of performance evaluation metrics calculated from all 100 measurements for the 10 μs pulse for interval (b).

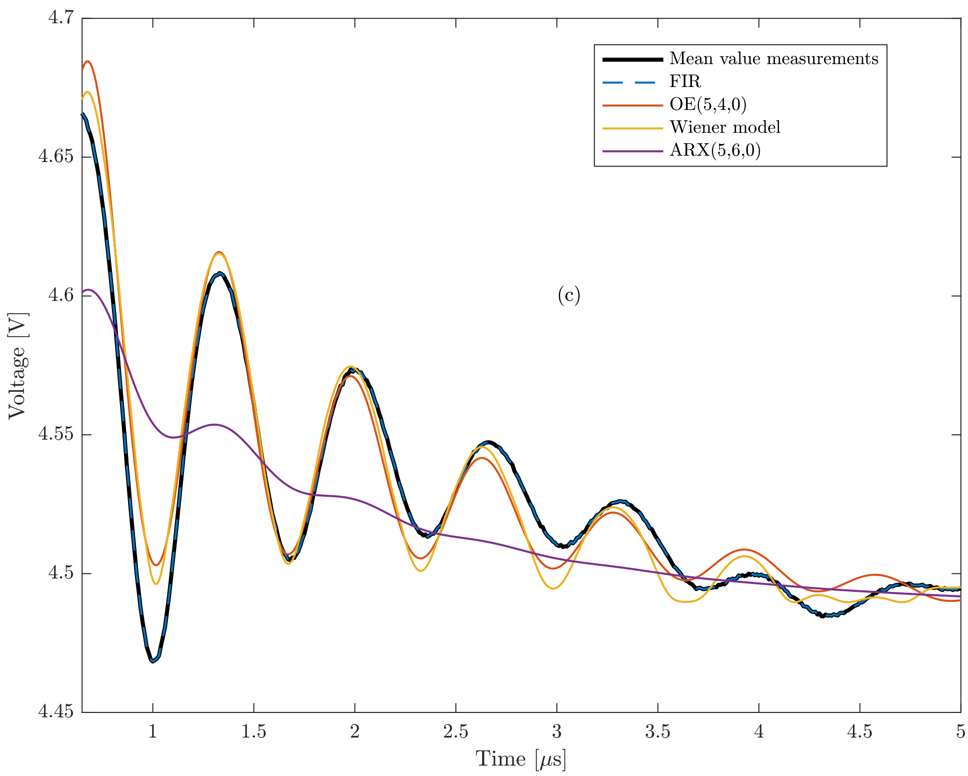

Figure 4.11: Simulated models together with mean value of the 100 measurements for the 10 μs pulse in interval (c).

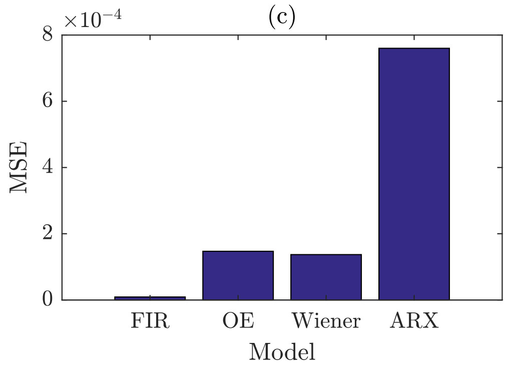

(a) MSE

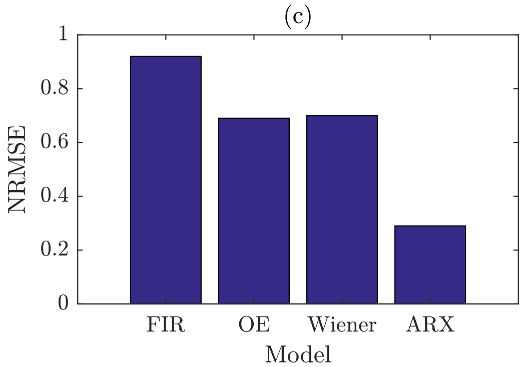

(b) NRMSE

Figure 4.12: Mean value of performance evaluation metrics calculated from all 100 measurements for the 10 μs pulse for interval (c).

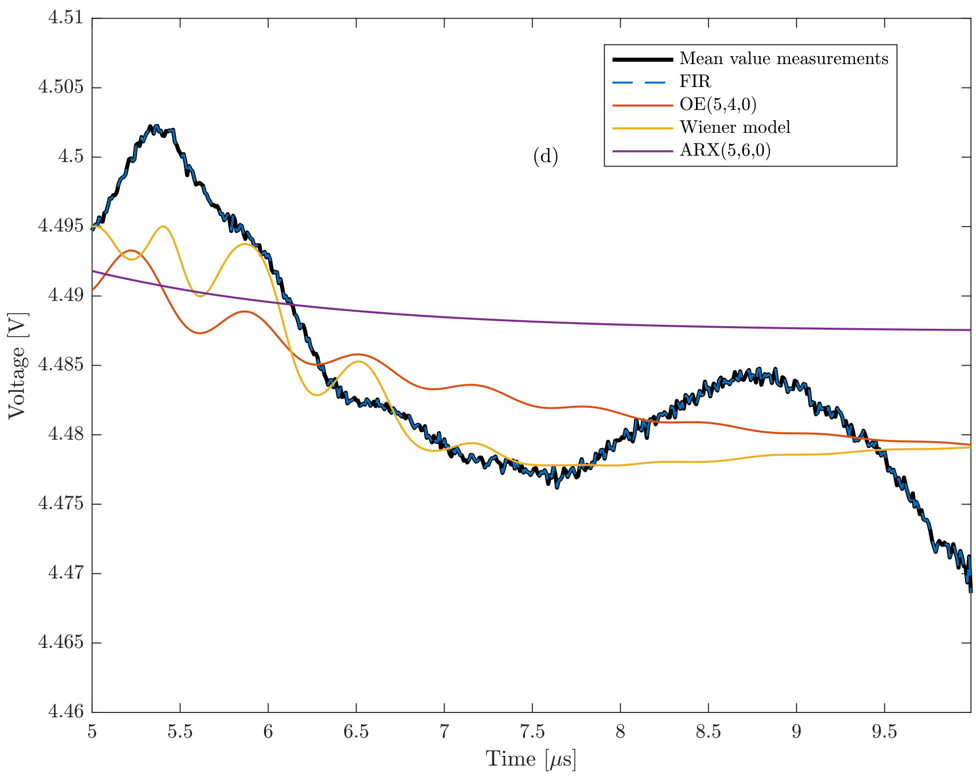

Figure 4.13: Simulated models together with mean value of the 100 measurements for the 10 μs pulse in interval (d).

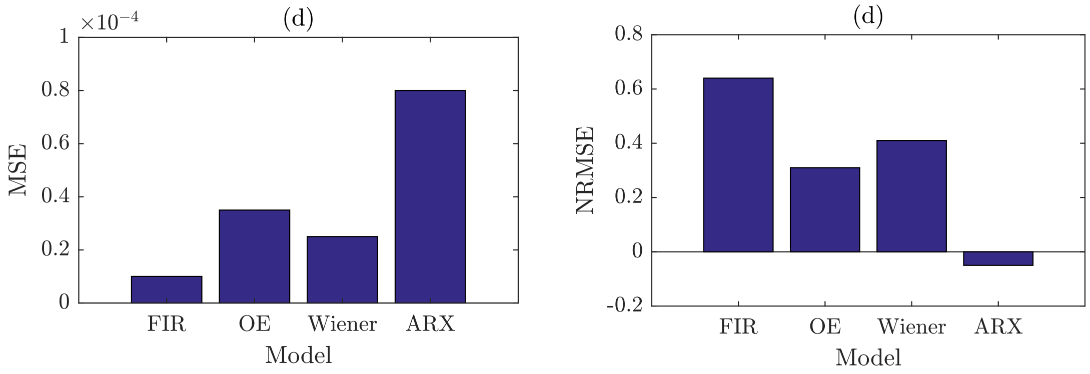

(a) MSE **(b)** NRMSE

Figure 4.14: Mean value of performance evaluation metrics calculated from all 100 measurements for the 10 μs pulse for interval (d).

4.6.2 Characteristics of the models

In the implementation of DPD, zeros of the PA model is of specific interest since some DPD algorithms analytically inverts the PA model to achieve the predistorted signal. In this case, it can be observed that the inverse PA models would be unstable since there are zeros outside the unit disc for all pole/zero maps in Figure 4.15. Hence, such algorithms would not be suitable for these models. Complex conjugated poles with a magnitude close to 1 will result in oscillations. From Figure 4.15b and 4.15c, it can be seen that there are three poles and zeros located very close to each other for both of the OE and the ARX. Comparing the values of the complex conjugated poles, the distance from the origin to each complex conjugated pole for the ARX is 0.982 whereas 0.992 for the OE, which explains why the oscillations for the ARX dies out faster.

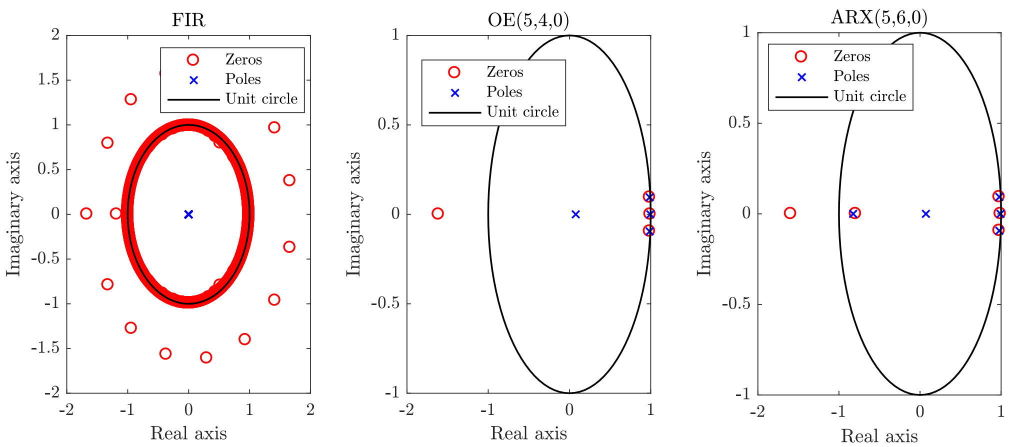

(a) FIR **(b)** OE **(c)** ARX

Figure 4.15: Pole/zero maps of FIR, OE and ARX for 10 μs pulse. Linear transfer function in Wiener model showed similar locations as the OE.

The transfer function of the OE is further investigated in by writing the expression as a sum of first and second order transfer functions using partial fraction expansions. The first order transfer functions comes from poles with only real part, whereas the second order transfer functions comes from complex conjugated poles. This expansion enables the possibility to study different components the whole transfer function consists of. In this case, it is desired to have at least one damped sinusoidal component, one exponential leading to the decaying behaviour and one response which gives the step. The partial fraction expansion lead to two second order transfer functions, one first order transfer function and one static gain, which can be written as

$$G(q) = \overbrace{\frac{r_1}{1 - p_1 q^{-1}}}^{TF1} + \overbrace{\frac{r_{2,1} + r_{2,2} q^{-1}}{1 - p_{2,1} q^{-1} - p_{2,2} q^{-1}}}^{TF2} + \overbrace{\frac{r_{3,1} + r_{3,2} q^{-1}}{1 - p_{3,1} q^{-1} - p_{3,2} q^{-1}}}^{TF3} + \overbrace{k}^{TF4}, \tag{4.17}$$

where r and p are scalar values which determines the zeros and poles locations of each transfer function and k is the static gain. In Figure 4.16 each transfer function has been simulated with the step input. The first and second transfer function shows an exponential and a damped sinusoidal, which was expected. Observing the fourth and third transfer function, it looks like their responses cancel some part of each other. However, when reducing the number of coefficients a good fit was not achieved. Also, by increasing the number of coefficients a better fit was not achieved. The same behaviours were achieved for the linear transfer function in the Wiener model.

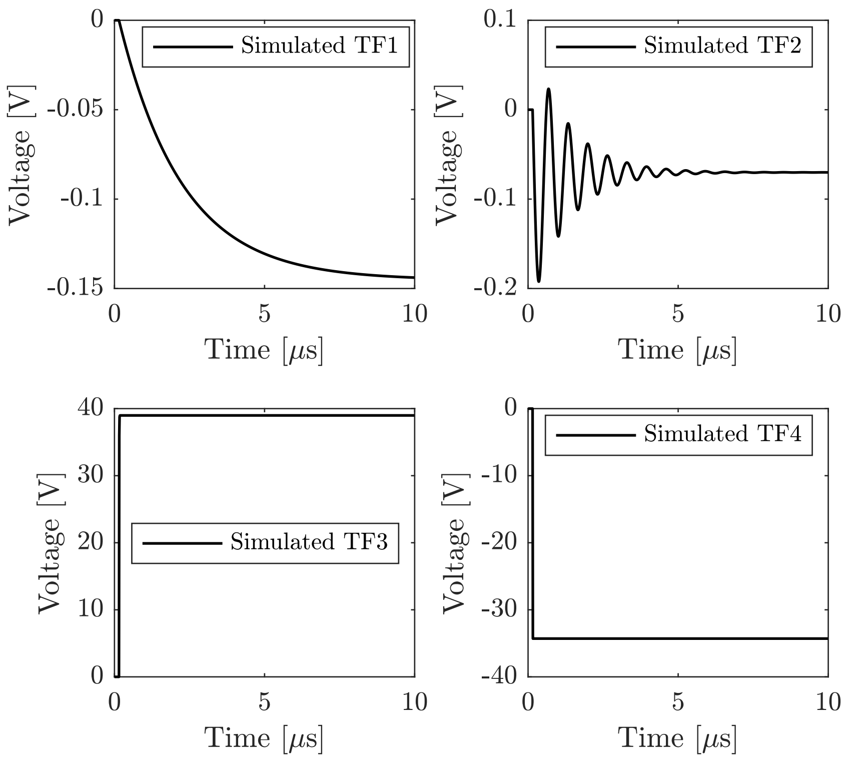

Figure 4.16: Partial transfer functions for the OE(5,4,0) simulated with the step input.

For the Wiener model, its linear transfer function and the nonlinearity are investigated in which are shown in Figure 4.17. The region for which the input to the nonlinearity varies between is marked with a rectangle. As can be seen, in that region the nonlinearity does not change a lot, instead it results in an output from the nonlinearity which is close to linear. Thereby it can further be concluded that the nonlinearity in this case is not necessary and instead the linear OE(5,4,0) model is sufficient.

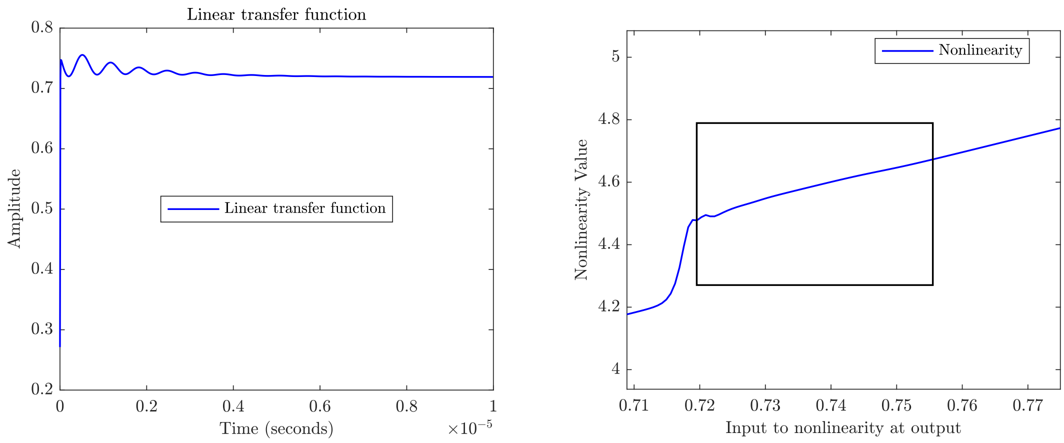

(a) Linear transfer function **(b)** Nonlinearity

Figure 4.17: Characteristics of Wiener model for the 10 μs pulse. The rectangle in 4.17b shows in which region the input to the nonlinearity varies in between.

4.7 Estimated models 100 μs pulse

From the models for the 10 μs pulse it could be concluded that models of the ARX type is not suitable for this application, since it is desired to have a model which performs good in simulation. Thereby, no further investigation in ARX models were performed for the 100 μs pulse. Instead three models has been estimated, one FIR model, one OE model and one Wiener model. The total number of coefficients for each linear transfer function are presented in Table 4.3. As can be seen, the number of coefficients for the FIR model is significantly increased compared to the number that was used for the 10 μs pulse.

Also here there is no input delay, as can be seen in the Figure 4.1b (lower) and the delay d is therefore 0 for all models. The same number of coefficients have been used for the OE and the Wiener model. For the Wiener model, a sigmoidnet with 10 units has been used as nonlinearity.

This section will go through the same evaluations for the models estimated for the 100 μs pulse as previously were performed for the 10 μs pulse. First simulations of the estimated models are shown together with the mean value of the measurements. Simulations of each model presented together with all measurements can be found in Appendix A. The simulations are divided into the performance evaluation intervals presented in Table 4.1 and the performance evaluation metrics are shown as bar graphs. In the bar graphs, a mean value of each metric calculated from all 100 measurements are presented. Additionally some characteristics of each model are also presented, e.g. pole/zero maps, partial transfer functions and the nonlinearity of the Wiener model.

Table 4.3: Number of coefficients for linear transfer functions for the models estimated for the 100 μs pulse.

Model / Coefficients	FIR	OE	Wiener
#	9999	9	9

4.7.1 Simulations

Simulations of the whole step are shown in Figure 4.18 and the corresponding performance evaluation metrics are shown in Figure 4.19. In terms of performance evaluation metrics it can be seen that the FIR performs the best. In contrast to the models estimated for the 10 μs pulse, it can be seen that the Wiener model performs much better than the OE for this pulse with longer duration.

Figure 4.20 and Figure 4.21 shows simulations and metrics for interval (b). The performance of the models is very similar, but the FIR performs best both from the simulation and the performance metrics.

For interval (c), depicted in Figure 4.22, it can be seen that the OE does not follow the oscillations. After 5 μs the most dominant oscillations have died out, meaning that only a minor part of the 100 μs data set includes the oscillations. Thereby this behaviour might be hard for a model to capture. Again the FIR performs best, according to the metrics presented in 4.23, but the performance of the Wiener model is also good.

The last interval (d) of the step is shown in Figure 4.24. Here it can be seen that the mean value from the measurements and the FIR is varying faster than the Wiener model. The Wiener model manages to capture the dynamics of lower frequencies in a desired way. The NRMSE and the MSE calculated from all measurements shows similar metrics for the FIR and the Wiener model. The metrics are shown in Figure 4.25. Further it can be seen that the OE does not give a desired behaviour neither in this interval.

To summarize, the FIR model performed the best in terms of lowest MSE and highest NRMSE for all intervals. In contrast to the 10 μs pulse, the nonlinear Wiener model is more suitable for this pulse whereas the OE did not achieve good performance. This shows that different model structures are needed for different PW.

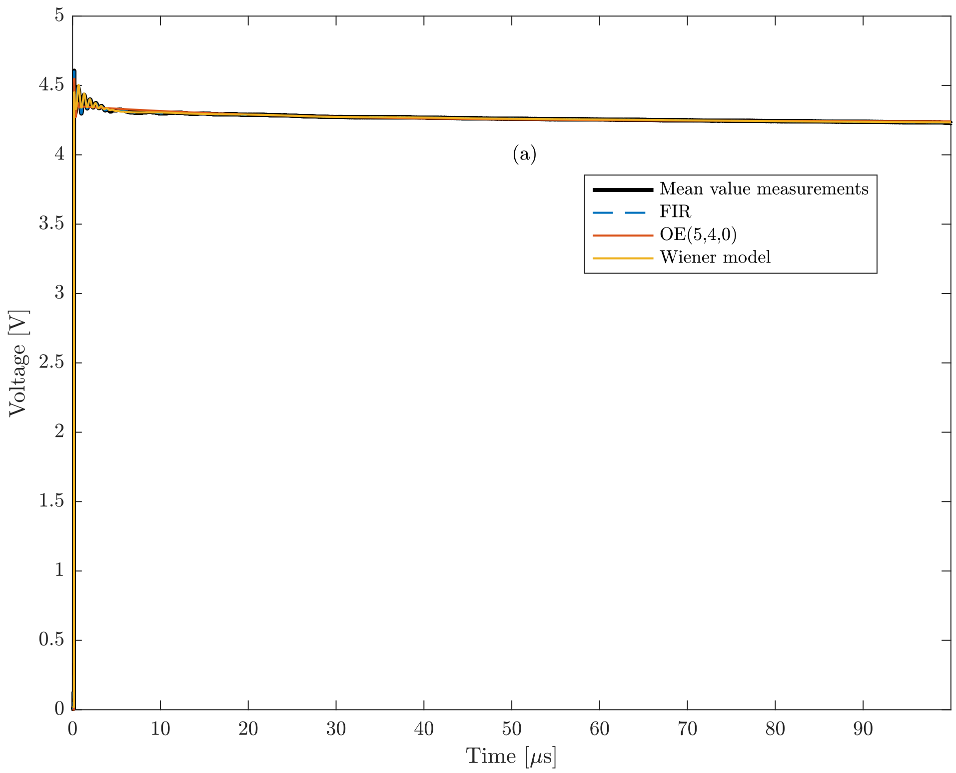

Figure 4.18: Simulated models together with mean value of the 100 measurements for the 100 μs pulse in interval (a).

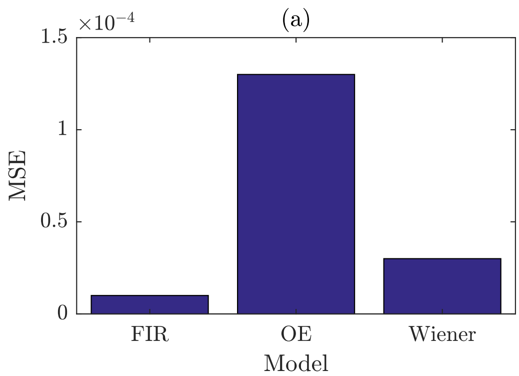

(a) MSE

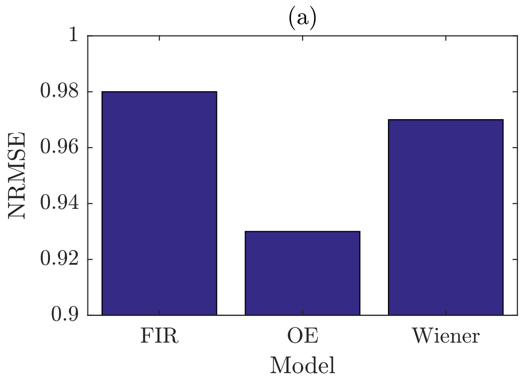

(b) NRMSE

Figure 4.19: Mean value of performance evaluation metrics calculated from all 100 measurements for the 100 μs pulse for interval (a).

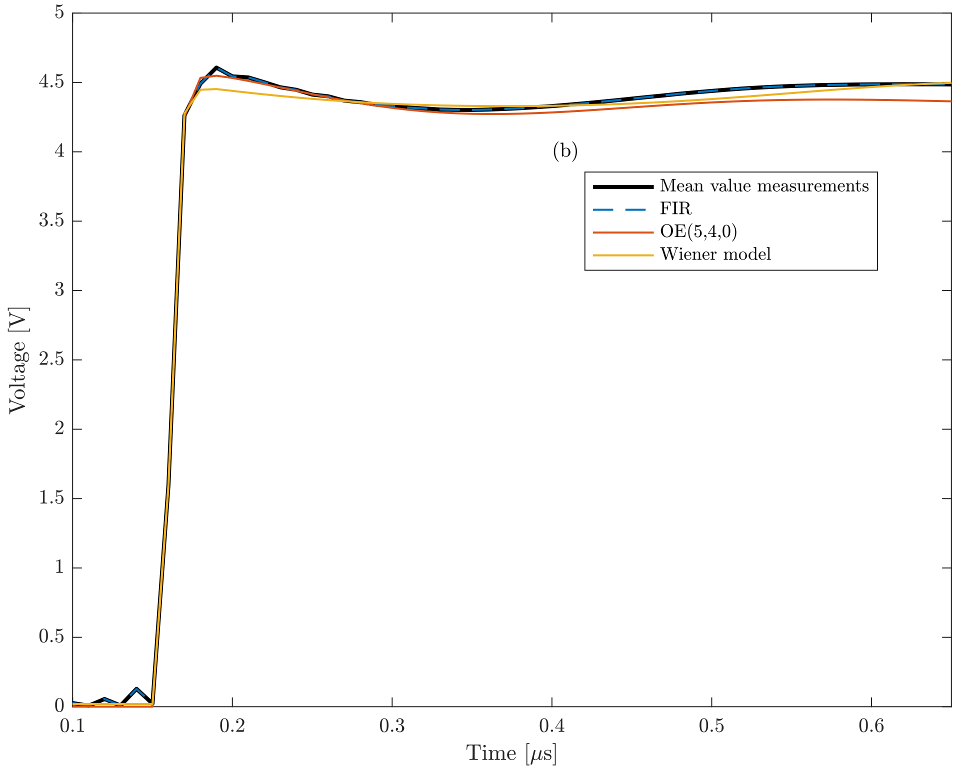

Figure 4.20: Simulated models together with mean value of the 100 measurements for the 100 μs pulse in interval (b).

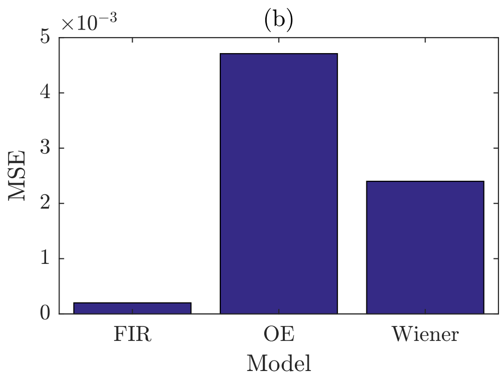

(a) MSE

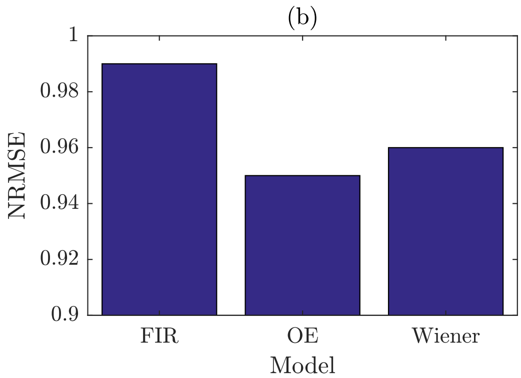

(b) NRMSE

Figure 4.21: Mean value of performance evaluation metrics calculated from all 100 measurements for the 100 μs pulse for interval (b).

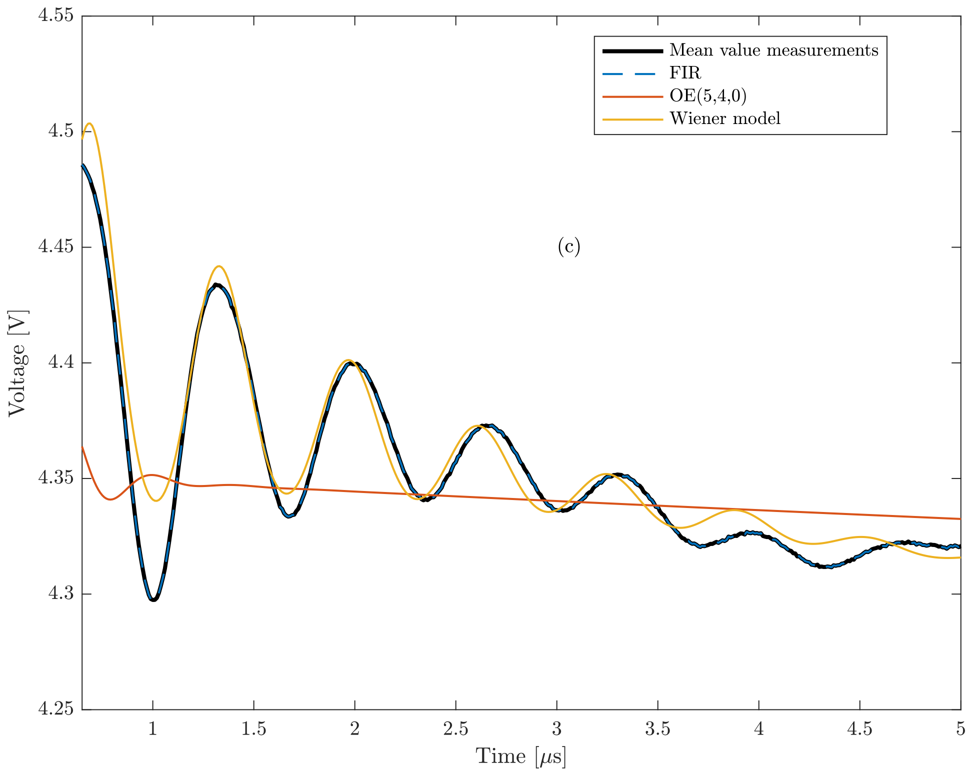

Figure 4.22: Simulated models together with mean value of the 100 measurements for the 100 μs pulse in interval (c).

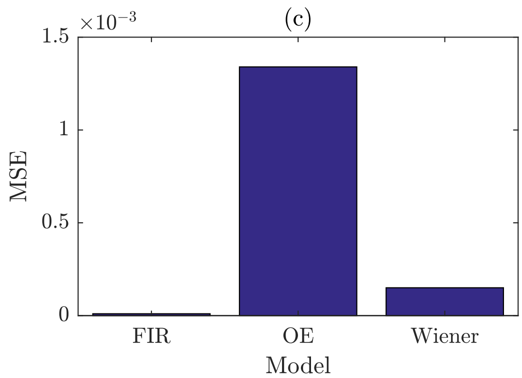

(a) MSE

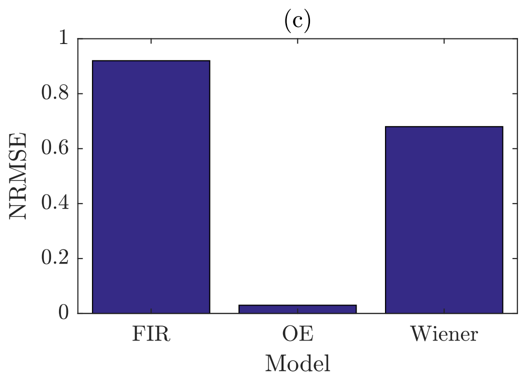

(b) NRMSE

Figure 4.23: Mean value of performance evaluation metrics calculated from all 100 measurements for the 100 μs pulse for interval (c).

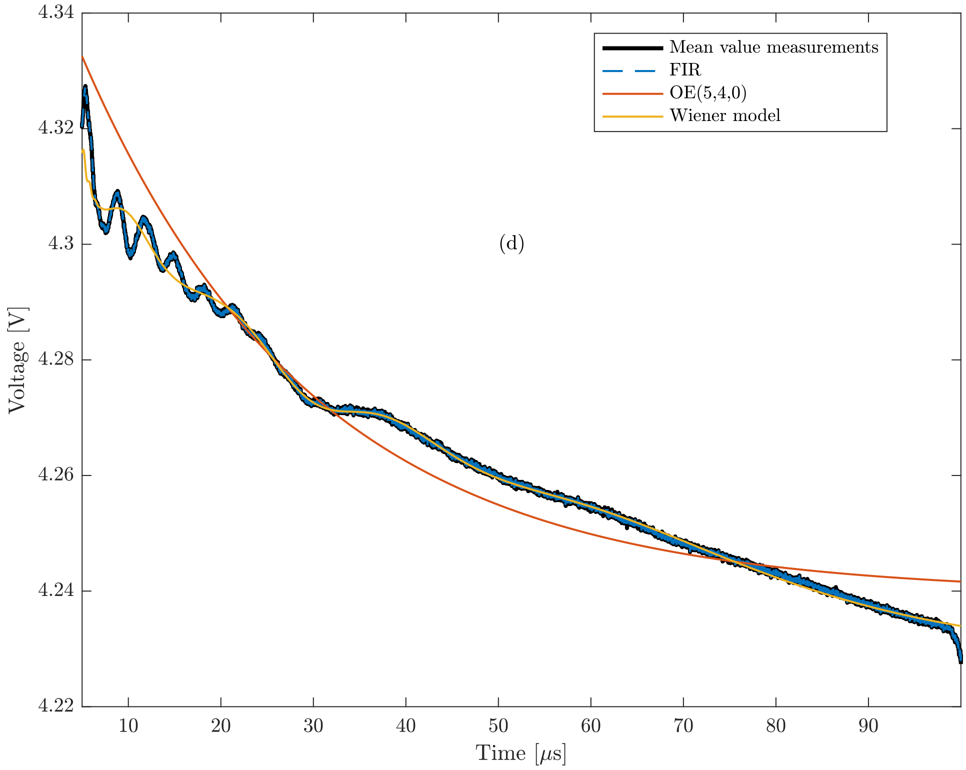

Figure 4.24: Simulated models together with mean value of the 100 measurements for the 100 μs pulse in interval (d).

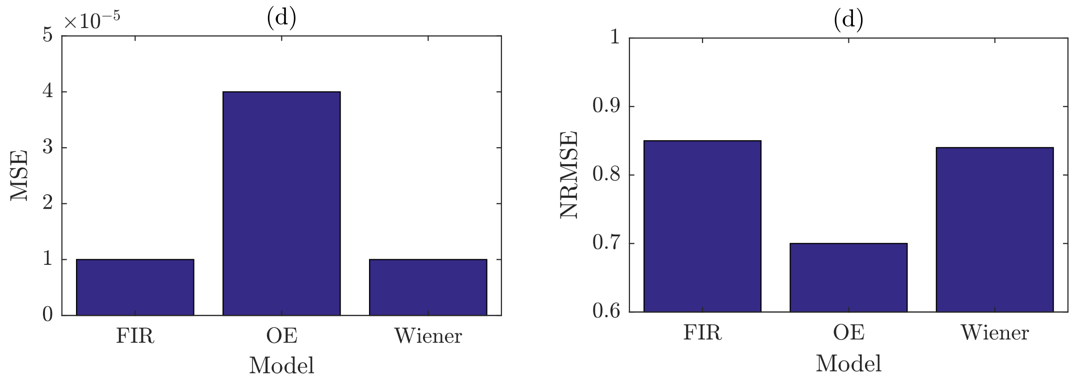

(a) MSE

(b) NRMSE

Figure 4.25: Mean value of performance evaluation metrics calculated from all 100 measurements for the 100 μs pulse for interval (d).

4.7.2 Characteristics of the models

From the pole/zero maps for the models estimated for the 100 μs pulse, similar observations as for the 10 μs pulse can be made. The map is depicted in Figure 4.26. All models have zeros with magnitude greater than one, implying that their inverse would be unstable. Also, by observing the distance of the complex conjugated poles from the origin of the OE and the Wiener, it could be seen that they have an absolute value of 0.95 for the OE whereas the linear transfer function for the Wiener model have an absolute value of 0.99. This again shows why the oscillations of the OE dies out faster than the oscillations in the Wiener model.

The partial transfer functions of the linear transfer function of the Wiener model showed similar behaviour as the the ones for the OE estimated for the 10 μs pulse, with one transfer function leading to a damped sinusoidal behaviour, one decaying function and then two steps. When decreasing the number of parameters in the model the performance got worse.

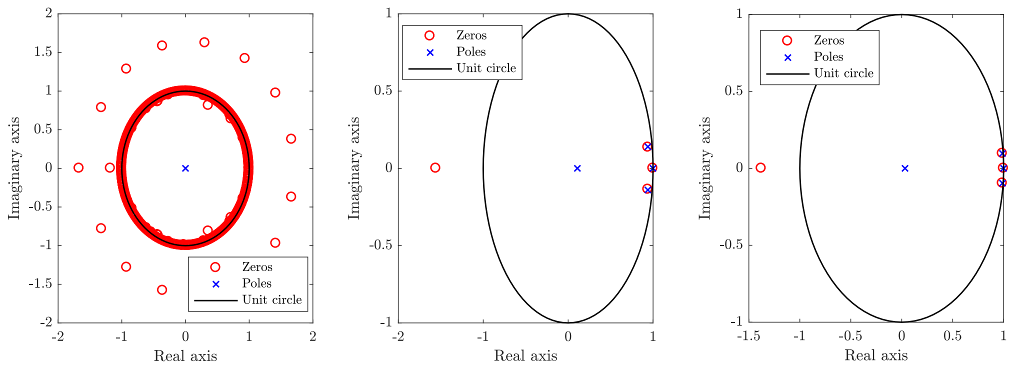

(a) FIR **(b)** OE **(c)** OE in Wiener model

Figure 4.26: Pole/zero maps of FIR, OE and Wiener model for 100 μs pulse.

Simulations have shown that for a PW of shorter duration, it is sufficient to use a linear OE model to describe the input-output relationship of a PA. For the longer pulse of 100 μs PW, it could be observed that the linear model did not manage to describe all dynamics that was of interest to capture. Instead, a nonlinear Wiener model proved to give better performance.

In Figure 4.27 the linear transfer function and the static nonlinearity are shown. By comparing the nonlinearity with its equivalent figure for the 10 μs pulse (Figure 4.17b), it can be seen that the 100 μs nonlinearity varies more depending on the input. By focusing on the input range for the nonlinearity, three transitions could be distinguished, where the nonlinearity goes from one input-output relation to another. Theses regions are illustrated in Figure 4.28. In the beginning of the linear transfer function the input to the nonlinearity is within the rectangle marked (1). Thereafter the slope is decreased in region (2) and in the end it is increased again in region (3).

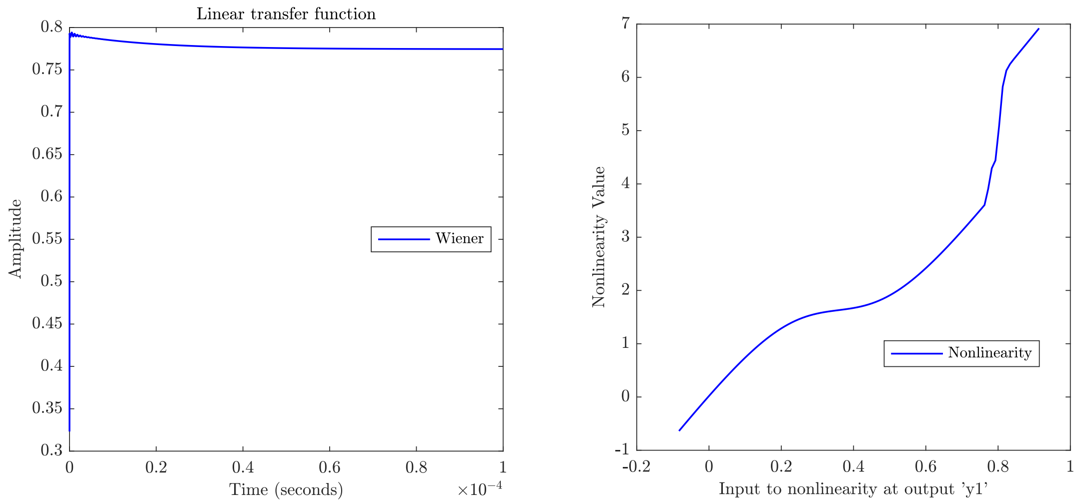

(a) Linear transfer function **(b)** Nonlinearity

Figure 4.27: Characteristics of Wiener model for the 100 μs pulse.

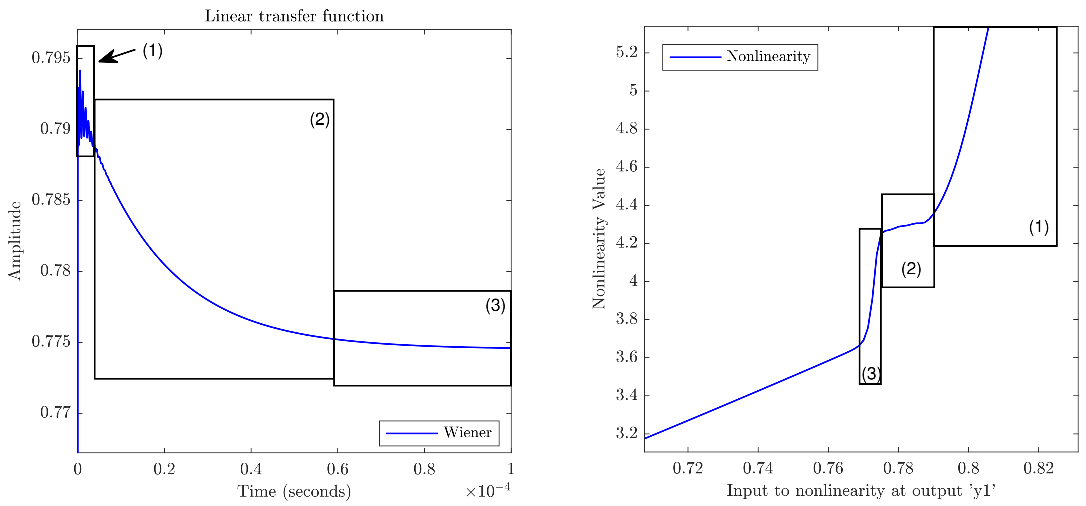

(a) Linear transfer function **(b)** Nonlinearity

Figure 4.28: Characteristics of Wiener model for the 100 μs pulse. The boxes illustrates how the nonlinearity changes for the different values that the linear transfer function gives as input to the nonlinearity. In the beginning of the linear transfer function the input to the nonlinearity is within the rectangle marked (1). Thereafter the slope is decreased in region (2) and in the end it is increased again in region (3).

5

Digital pre-distortion

This chapter introduces the DPD technique that have been used to achieve a desired output and compensate for the transients present in the PA output which could be seen from measurements. First, the concept of DPD is reviewed. Thereafter, the ILC scheme is introduced which is the DPD algorithm that has been implemented. Performance evaluation for the DPD is introduced and the chapter ends with results from when the DPD is implemented, first in simulation and thereafter in experiments.

5.1 Concept of DPD

The idea with DPD and pulse shaping techniques are to pre-compensate for undesired behaviour by introducing a block in the chain which includes the inverse behaviour of the system. Thereby the desired output signal can be sent to the DPD, which in turn generates a predistorted input signal, resulting in a desired output response from the PA. As could be seen from the measurements, when a pulse was used as input to the PA its response included transients, similar to Figure 1.1a in the Introduction. By implementing a DPD, another block will be introduced, which will take the desired output response as input. The DPD then generates the predistorted input that will drive the PA response to its desired shape. This is depicted in Figure 1.1b.

DPD is well-used in communication system, commonly used to compensate for the nonlinear distortion introduced. In such applications the PA is operating in its nonlinear regime, hence a nonlinear model must be used for the PA. Inverting a nonlinear model can be complex to perform analytically, and instead often system identification tools are used to identify an inverse model of the PA [12]. Examples of such algorithms are the indirect learning architecture (ILA) [19] and the model-based indirect learning architecture (MILA) [20] where an inverse model of the PA is estimated after an input has been fed to the PA and its response has been measured. The goal is thereby to find $x = f(y)$.

In this research, the PA has been operating in its linear regime focusing instead on memory effects. From the modelling it could be seen that a nonlinear Wiener model still might be needed for the 100 μs pulse. The other model structures that were investigated in were linear, hence their inverse models are straight forward to find. The only requirement is stability which means that the zeros of the PA model must be within the unit circle, which would imply that the poles of its inverse model is within the unit circle. In the modelling it could be seen that the models had zeros outside the unit disc, and thus it would not be possible to implement the inverse of the estimated models as a predistorter.

As reviewed in the introduction, a DPD algorithm that focuses on compensating for interpulse instabilities is presented in [13]. This algorithm is however not suitable for this application since the focus here is to compensate effects in the pulse, whereas the presented algorithm uses the mean value of the amplitude for each pulse to achieve the same characteristics for every pulse within a CPI.

5.2 Iterative learning control

A DPD algorithm presented in [12] is the the ILC. The purpose of the implementation of a predistorter is to find the input signal that will drive the system to a desired output y_d. In ILC this optimal input signal is estimated through an iterative process. The algorithm requires that the desired output response is the same for each iteration, and for pulsed radar signals this is suitable.

A block diagram of the ILC scheme is shown in Figure 5.1, where n is the discrete time index, k is the iteration of the algorithm, u is the predistorted input signal, y is the PA output response, y_d is the desired PA output response and e is the error between actual and desired output response. The ILC algorithm uses the observed error between the actual output and the desired output, and then updates the input for the next iteration u_{k+1}. The iterations continues until a desired behaviour for the output is achieved.

Two different ILC algorithms have been proposed in [21], namely the gain based and the linear. In this thesis the gain based schedule have been used. The ILC algorithm then updates the input signal for the next iteration according to

$$u_{k+1}(n) = u_k(n) + g_k^{-1}(n)e_k(n), \tag{5.1}$$

where $g_k(n) = y_k(n)/u_k(n)$ and $e_k(n) = y_d(n) - y_k(n)$.

Only the error that occurs when the PA is on is of interest and therefore the input signal is only changed during that period. From the initial measurements in Figure 3.6 and Figure 3.7, it could be observed that the pulse had reached its top after approximately 0.17 μs and it ended after 9.99 μs for the 10 μs pulse and after 99.99 μs for the 100 μs pulse. Therefore the error will only be compared for this time period, which implies that the baseband input signal only will be changed for this period.

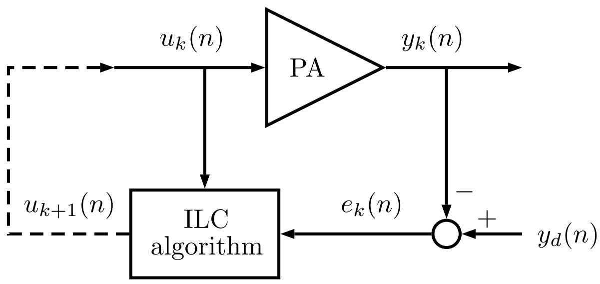

Figure 5.1: Block diagram illustrating the iterative learning control scheme.

5.3 Performance evaluation

In order to evaluate the performance of the predistorter, MSE will be used. Its mathematical formula can be found in (4.15). For the DPD, the evaluation will be to compare the measured output response with the desired response as depicted in Figure 5.2. The performance will not be evaluated for the whole pulse. Instead, only the response for where the error is calculated will be taken into consideration, since for all other time instances that PA is off. Similar as for the performance evaluation for the modelling part, the response are divided into four intervals. The only difference here is that the performance evaluation starts at time 0.17 μs since the error will only be calculated from that time until the end of each pulse.

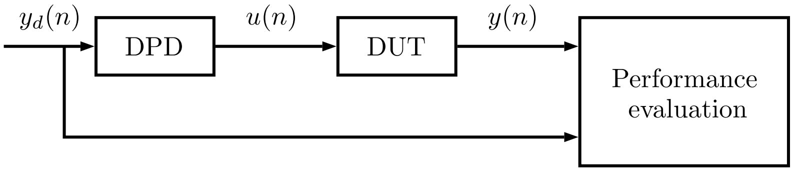

Figure 5.2: Performance evaluation for the DPD. The desired output response is fed to the DPD which gives the predistorted input signal that is sent to the DUT. The output response from the DUT and the desired output response is thereafter compared.

5.4 ILC in simulation

The ILC algorithm was first tested in simulation, and thereafter implemented in experiments. In the simulations, the impulse response models were used. The other model structures were also tested, but since the FIR models achieved best performance evaluation metrics they will be presented. Similar results were however achieved for the other model structures as well. The desired output signal that have been selected have an amplitude of 4.48 V for the 10 μs pulse and an amplitude of 4.28 V for the 100 μs pulse.

5.4.1 10 μs pulse

In Figure 5.4 four iterations with the ILC in simulation are shown. Each row represents a new iteration in the algorithm, and the columns represents different intervals of the pulse. It can be seen that ILC manages to eliminate the undesired behaviour after three iterations. In Table 5.1 the MSE is presented for each iteration and interval. Here it can be seen that no further improvement after the third iteration. In Figure 5.3 the adapted input signal are shown together with the error. The evolution of the input signal shows that in order to achieve a desired shape of the output signal one must predistort the input signal such that its behaviour is out of phase with the undesired transients.

Table 5.1: MSE between desired output and simulated output for different intervals and iterations for the 10 μs pulse in simulation. The values have been scaled with a factor 10^3 to increase readability.

Iteration \ Interval	0.17-9.99 μs	0.17-0.65 μs	0.65-5 μs	5-9.99 μs
$k = 1$	2.38	17.12	3.45	0.07
$k = 2$	0.04	0.58	0.02	0.001
$k = 3$	0.01	0.29	0.0001	0.0002
$k = 4$	0.01	0.29	0.0001	0.0002

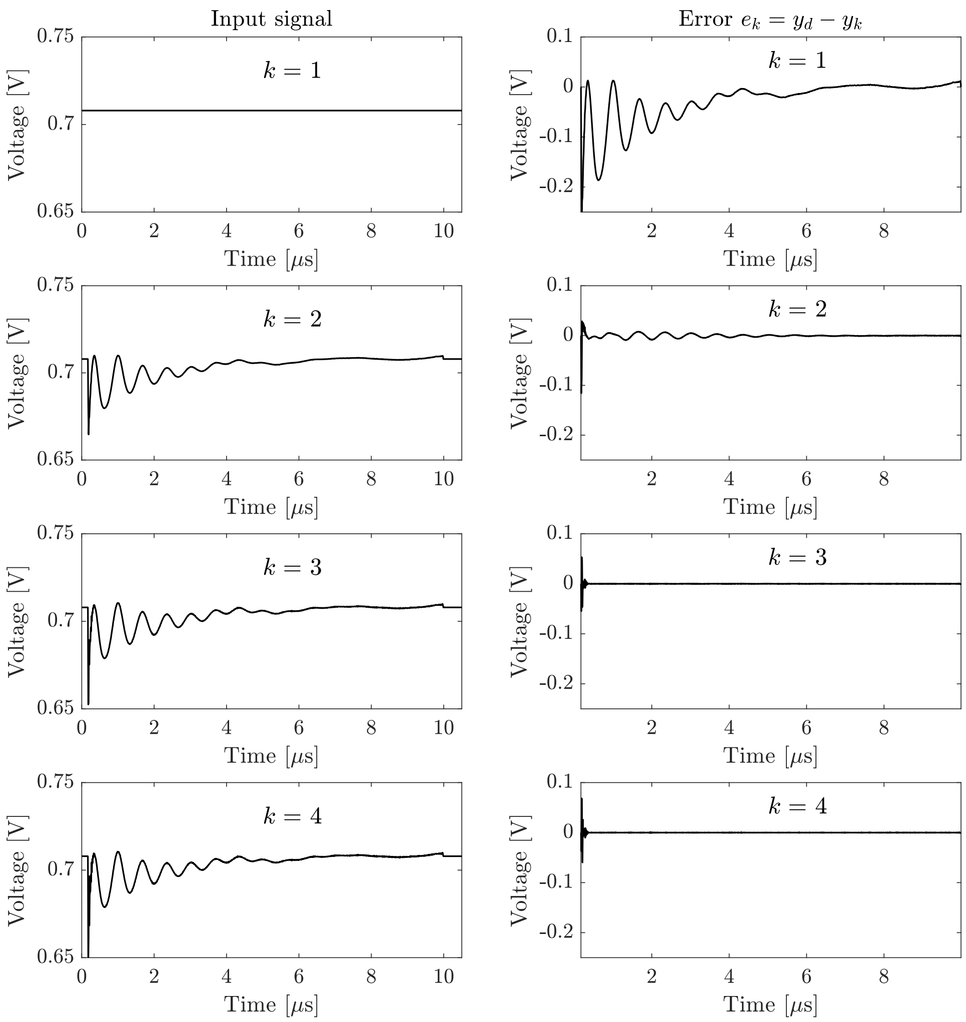

Figure 5.3: ILC in simulation for the 10 μs pulse, error observed between 0.17 and 9.99 μs. First column shows the input signal from ILC and second column shows the error achieved between the desired output and measured output.

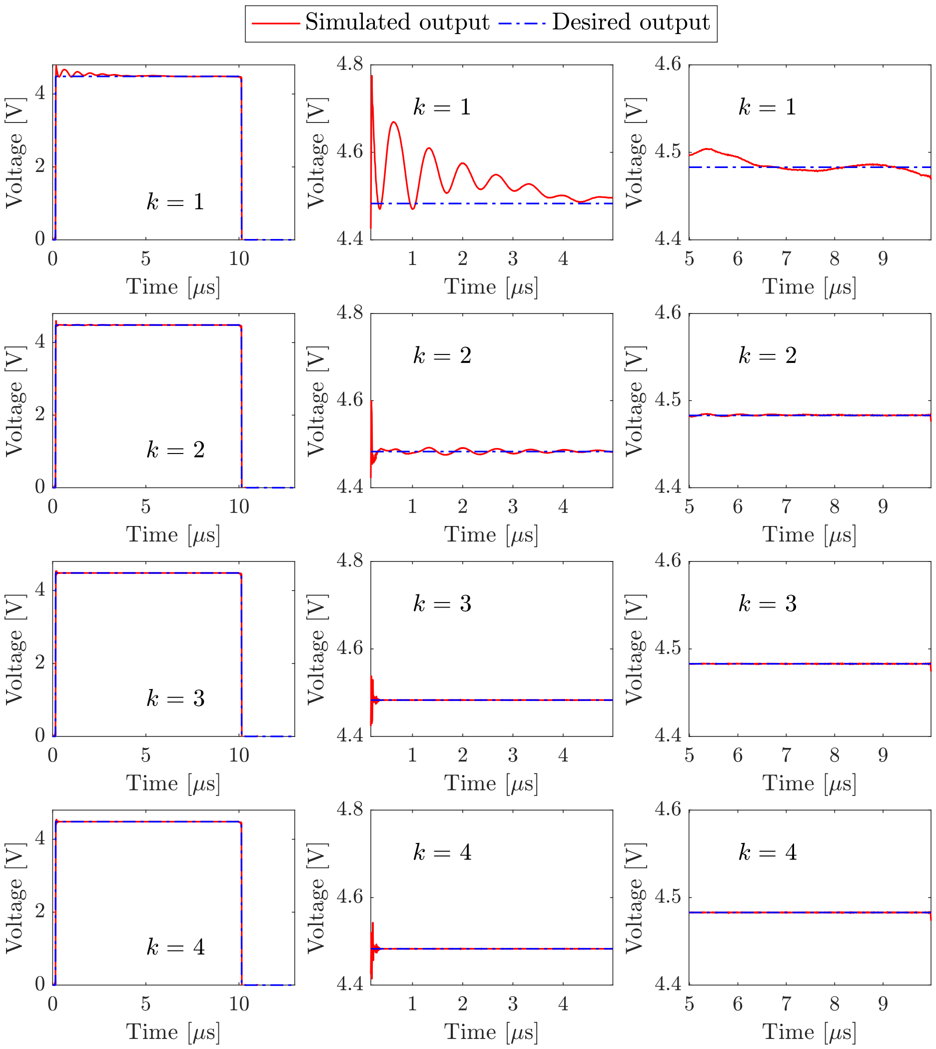

Figure 5.4: ILC implemented in simulation for the 10 μs pulse. The first column shows the whole pulse, in the middle the oscillating transients and the last column shows the last part of the pulse. Each row represent a new iteration in ILC. The DPD manages to successfully compensate for the undesired behaviour with three iterations. This can be seen by observing the iterations in the second column where the simulated output follows the desired output for iteration $k = 3$. Also it can be observed that no further improvement is achieved after the third iteration.

5.4.2 100 μs pulse

In Figure 5.6 four iterations with the ILC in simulation are shown for the 100 μs pulse. Each row represents a new iteration in the algorithm, and the columns represents different intervals of the pulse. Similar as for the 10 μs pulse, ILC manages to eliminate the undesired behaviour after three iterations. In Table 5.2 the MSE is presented for each iteration and interval. In Figure 5.5 the adapted input signal are shown together with the error. The same observation as for the 10 μs pulse can be made.

Table 5.2: MSE between desired output and simulated output for different intervals and iterations for the 100 μs pulse in simulation. The values have been scaled with a factor 10^3 to increase readability.

Iteration \ Interval	0.17-99.99 μs	0.17-0.65 μs	0.65-5 μs	5-99.99 μs
$k = 1$	1.04	22.37	6.85	0.7
$k = 2$	0.001	0.06	0.02	0.0002
$k = 3$	0.0002	0.03	0.0001	0.0001
$k = 4$	0.0002	0.03	0.0001	0.0001

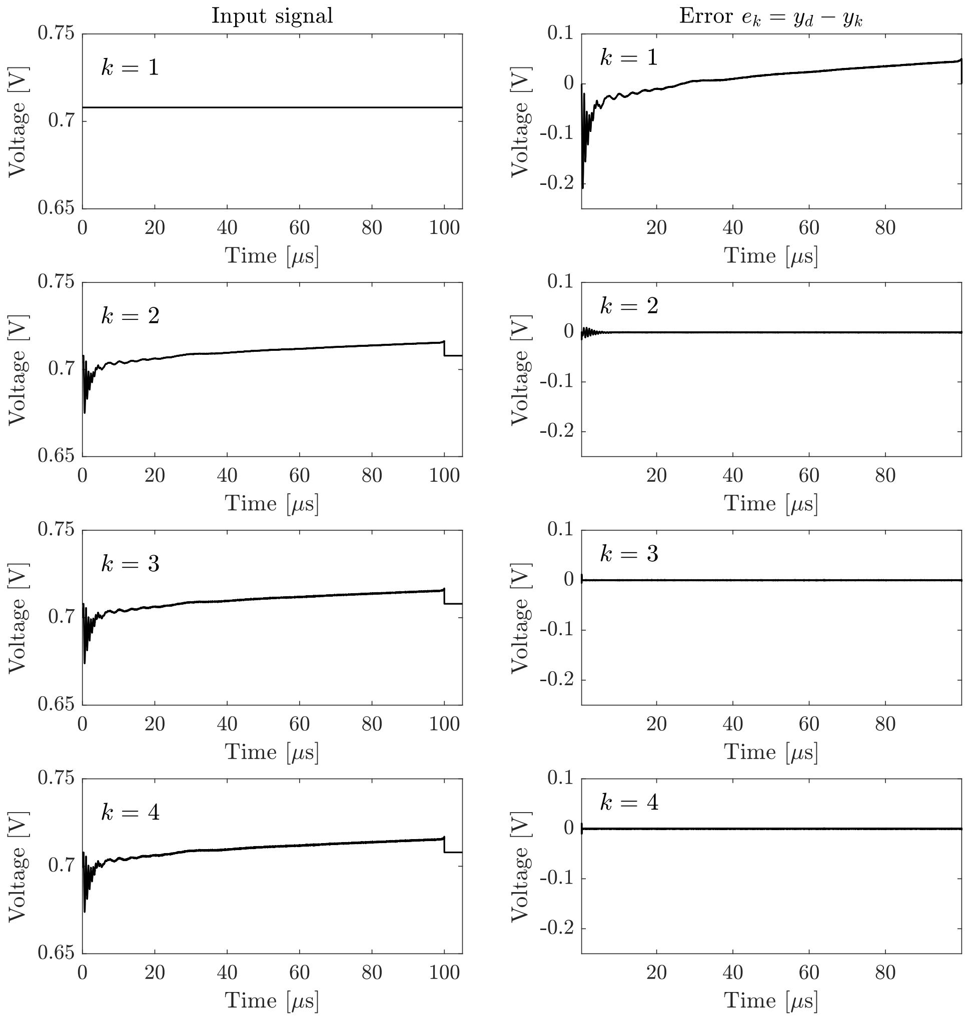

Figure 5.5: ILC in simulation for the 100 μs pulse, error observed between 0.17 and 9.99 μs. First column shows the input signal from ILC and second column shows the error achieved between the desired output and measured output.

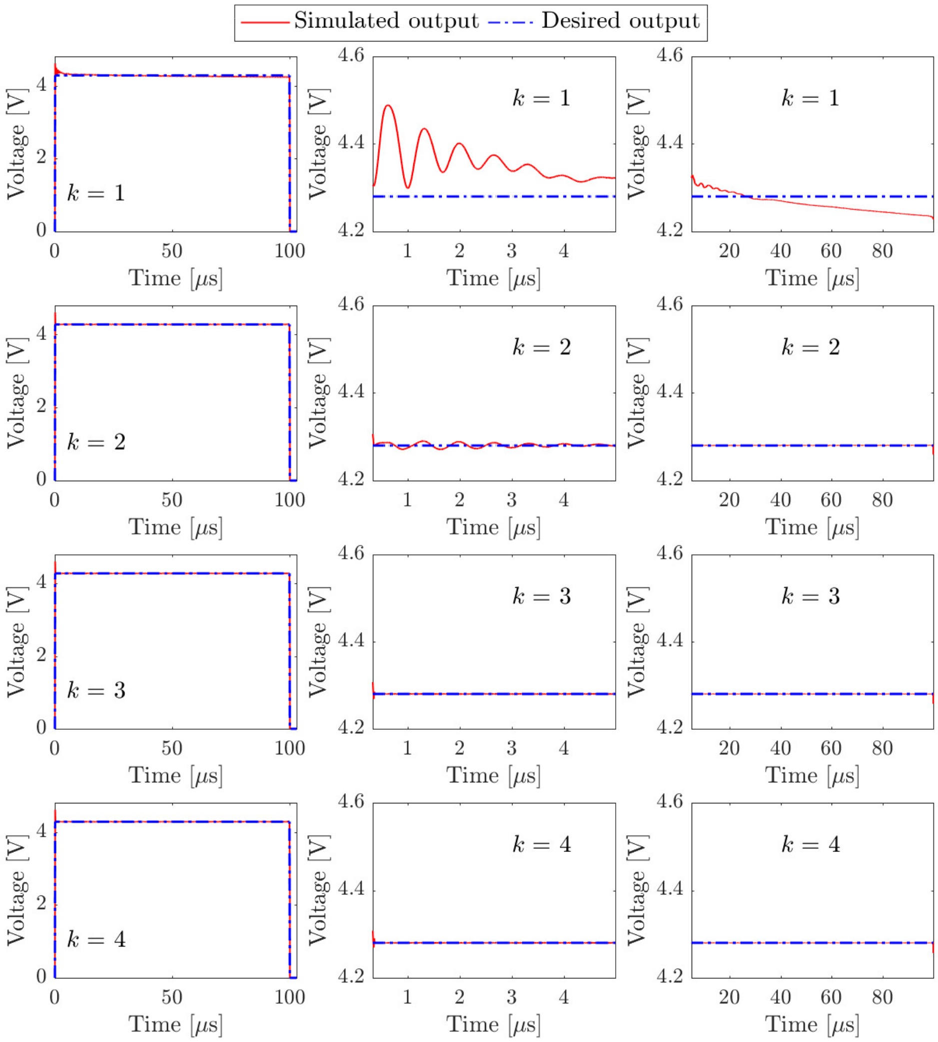

Figure 5.6: ILC implemented in simulation for the 100 μs pulse. The first column shows the whole pulse, in the middle the oscillating transients and the last column shows the last part of the pulse. Each row represent a new iteration in ILC. The DPD manages to successfully compensate for the undesired behaviour with three iterations. This can be seen by observing the iterations in the second column where the simulated output follows the desired output for iteration $k = 3$. Also it can be observed that no further improvement is achieved after the third iteration.

5.5 ILC in experiments

When the ILC are implemented in experiments the algorithm will start to compensate for the noise, meaning that the input signal will include more and more noise. An attempt to first generate the optimal input signal in simulation and thereafter apply that input in experiments was therefore performed. As could be seen from the initial measurements the measurement did not start exactly at the same time for every measurement. Thereby, when the optimal input signal was generated in simulation and applied on the real system further iterations were still needed to compensate for the oscillating transients and it proved to be more successful to only iterate in experiments. The gain can also differ depending on temperature etc. and therefore the amplitude of the measured output can differ from the simulation which made it more advantageous to directly iterate in the experiments. The model are however still used in each iteration to check the expected output for the new input. This way the risk of feeding an input signal that might damage any part in the setup is minimized.

The same desired output signals as in simulation have been used, namely an amplitude of 4.48 V for the 10 μs pulse and an amplitude of 4.28 V for the 100 μs pulse.

5.5.1 10 μs pulse

Figure 5.8 shows four iterations with the ILC in experiments for a 10 μs pulse. By observing the last column (5-9.99 μs) in Table 5.3 it can be seen that the measured response includes more noise for iteration 4 than for iteration 3. This is because the algorithm tries to compensate for the measurement noise, leading to a noisier input signal. This can further be seen by observing the input signal used, presented in Figure 5.7. Another observation that can be made is that the error from 0.17-0.65 μs was increased for almost every iteration. This probably comes from problems with timing. The time for which the error was calculated for was therefore decreased to start at 0.33 μs instead, which improved the performance according to Table 5.4. From the response depicted in Figure 5.9 it can be seen that it is not possible to fully compensate for the oscillating transients, which also is due to timing problems. Similar as in simulation no improvement is achieved after the third iteration. The input signal used and the error achieved are shown in Figure 5.10.

Table 5.3: MSE between desired output and measured output for different intervals and iterations when the error has been compared from 0.17-9.99 μs for the 10 μs pulse in experiment. The values have been scaled with a factor 10^3 to increase readability.

Iteration \ Interval	0.17-9.99 μs	0.17-0.65 μs	0.65-5 μs	5-9.99 μs
$k = 1$	2.51	17.25	3.70	0.10
$k = 2$	3.09	52.59	0.76	0.26
$k = 3$	2.81	51.47	0.51	0.04
$k = 4$	5.47	104.72	0.49	0.08

Table 5.4: MSE between desired output and measured output for different intervals and iterations when the error has been compared from 0.33-9.99 μs for the 10 μs pulse in experiment. The values have been scaled with a factor 10^3 to increase readability.

Iteration \ Interval	0.33-9.99 μs	0.33-0.65 μs	0.65-5 μs	5-9.99 μs
$k = 1$	1.99	16.06	3.21	0.07
$k = 2$	0.59	5.78	0.64	0.21
$k = 3$	0.28	2.90	0.38	0.03
$k = 4$	0.33	4.69	0.31	0.67

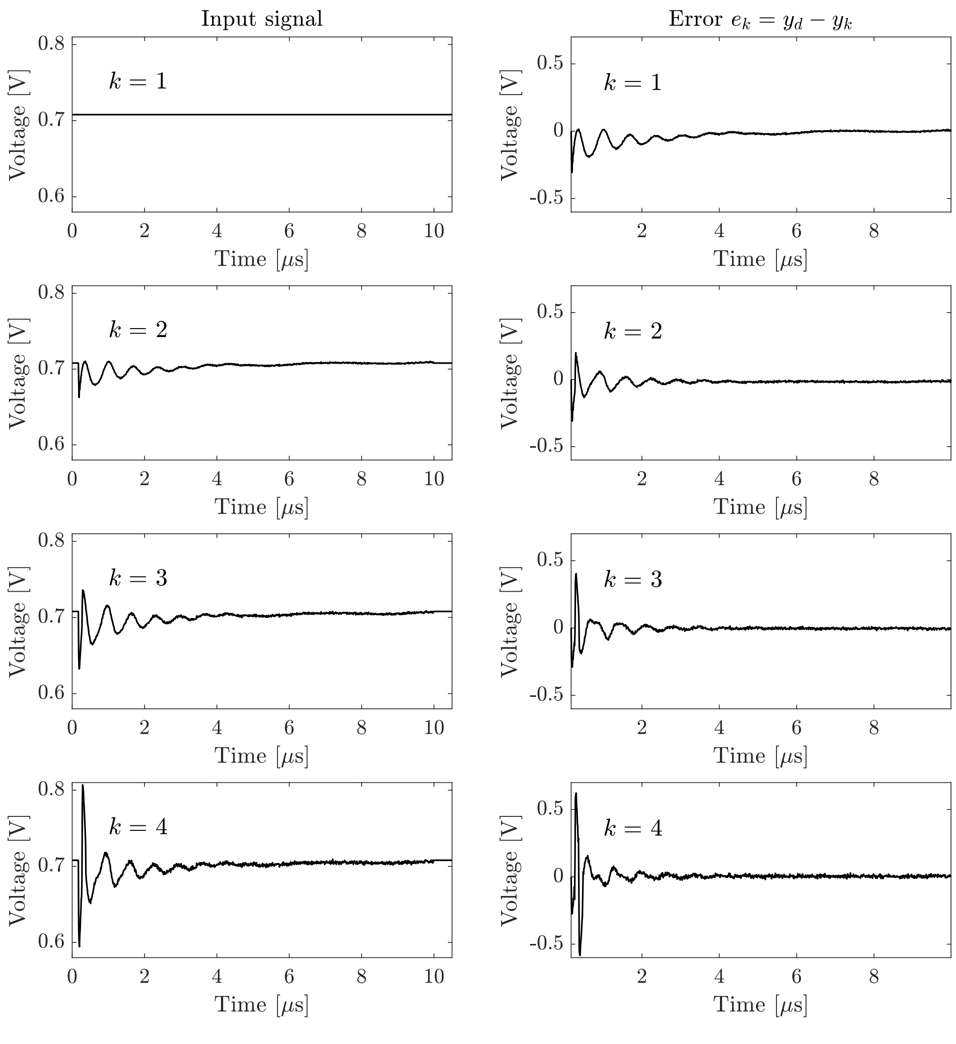

Figure 5.7: ILC in experiments for the 10 μs pulse, error observed between 0.17 and 9.99 μs. First column shows the input signal from ILC and second column shows the error achieved between the desired output and measured output.

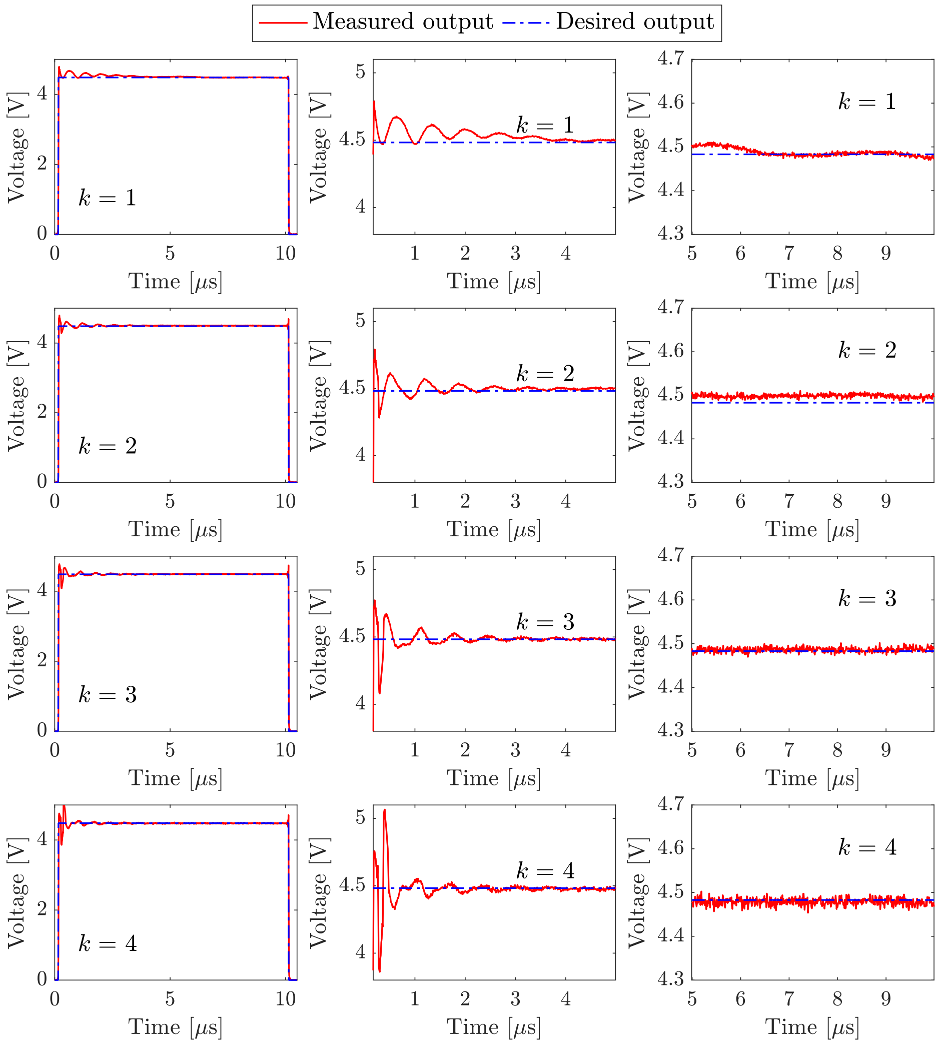

Figure 5.8: ILC implemented in experiment for the 10 μs pulse where the error has been evaluated at 0.17-9.99 μs. The first column shows the whole pulse, in the middle the oscillating transients and the last column shows the last part of the pulse. Each row represent a new iteration in ILC. It can be seen that the oscillating transients becomes worse from the second column, but in the end of the pulse a desired amplitude of the pulse is achieved which can be seen from iteration $k = 3$ in the last column, where the measured output follows the desired output.

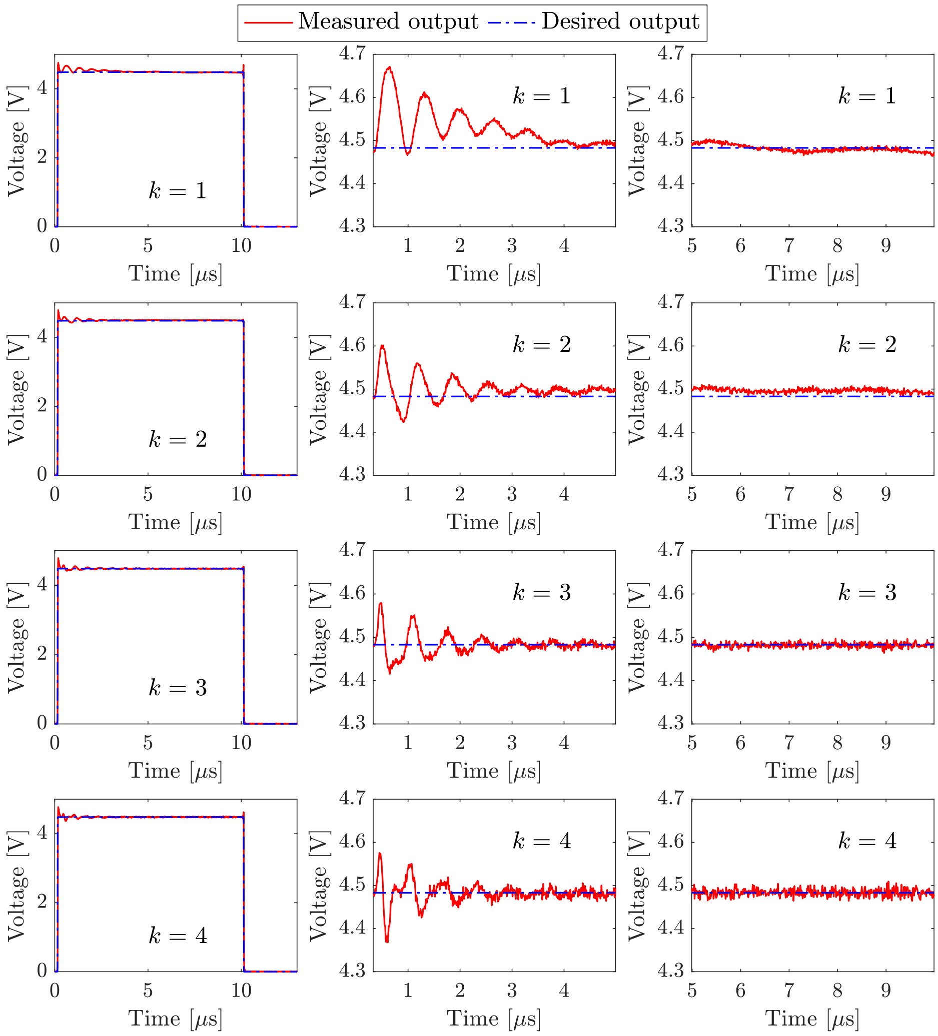

Figure 5.9: ILC implemented in experiment for the 10 μs pulse where the error has been evaluated at 0.33-9.99 μs. The first column shows the whole pulse, in the middle the oscillating transients and the last column shows the last part of the pulse. Each row represent a new iteration in ILC. Comparing the result with Figure 5.8 an improvement is achieved for the oscillating transients, but there are still some undesired behaviour which can be seen in the second column where the measured output does not follow the desired output for any iteration. In the end of the pulse the desired amplitude is achieved which is seen in the last column where the measured output follows the desired output after iteration $k = 3$.

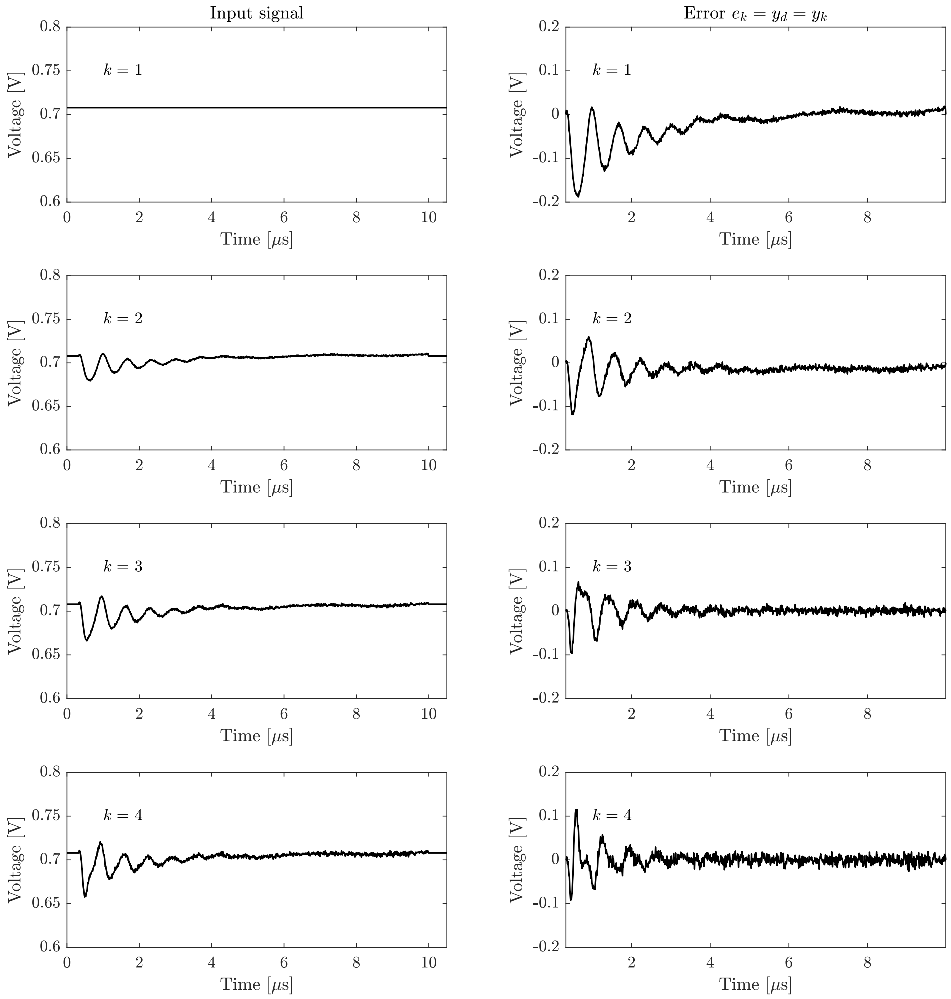

Figure 5.10: ILC in experiments for the 10 μs pulse, error observed between 0.33 and 9.99 μs. First column shows the input signal from ILC and second column shows the error achieved between the desired output and measured output.

5.5.2 100 μs pulse

Previous results have shown that no further improvement are achieved after three iterations, thereby when evaluating the 100 μs pulse in experiments only three iterations are shown. Also since the 10 μs pulse showed that it advantageous to compare the error from 0.33 μs, this has been used here as well.

Similar as for the 10 μs pulse, the oscillating transients remains after applying the algorithm as can be seen in Figure 5.11. However, the decaying behaviour is successfully compensated for in this case. The MSE is presented in Table 5.5 and the input signal and the error are depicted in Figure 5.12.

Table 5.5: MSE between desired output and measured output for different intervals and iterations for the 100 μs pulse in experiment. The values have been scaled with a factor 10^3 to increase readability.

Iteration \ Interval	0.33-99.99 μs	0.33-0.65 μs	0.65-5 μs	5-99.99 μs
$k = 1$	0.96	27.61	9.34	0.49
$k = 2$	0.05	4.78	0.42	0.02
$k = 3$	0.05	2.30	0.39	0.03

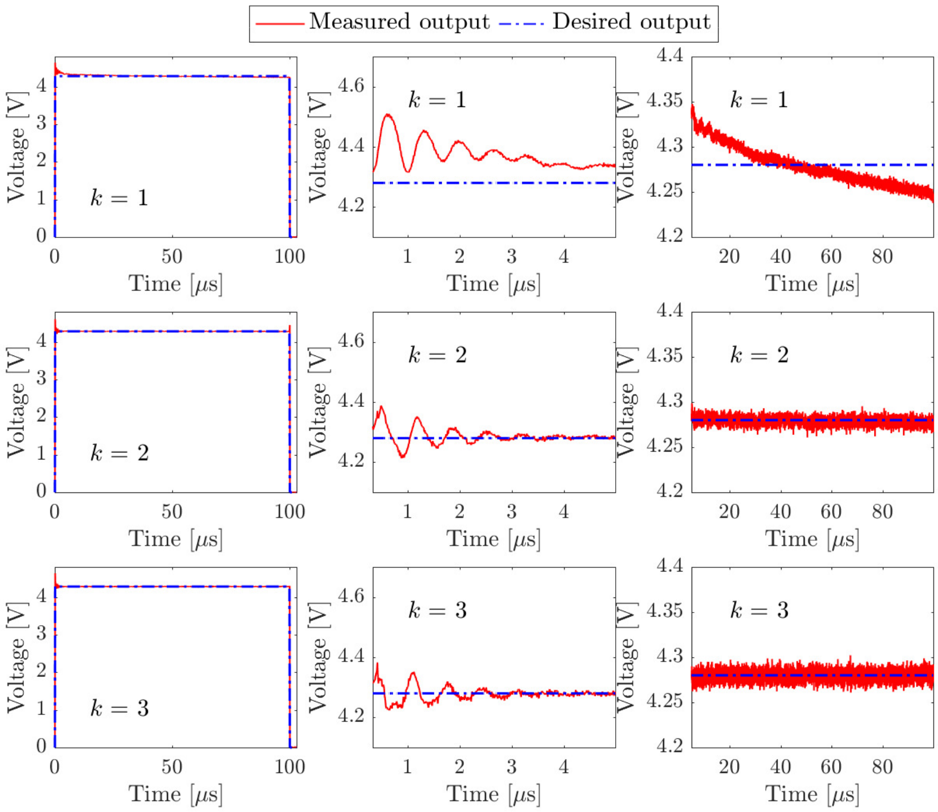

Figure 5.11: ILC implemented in experiment for the 100 μs pulse where the error has been evaluated at 0.33-9.99 μs. The first column shows the whole pulse, in the middle the oscillating transients and the last column shows the last part of the pulse. Each row represent a new iteration in ILC. Similar as for the 10 μs pulse there are still some undesired behaviour which can be seen in the second column where the measured output does not follow the desired output for any iteration. In the end of the pulse the desired amplitude is achieved which is seen in the last column where the measured output follows the desired output after iteration $k = 2$.

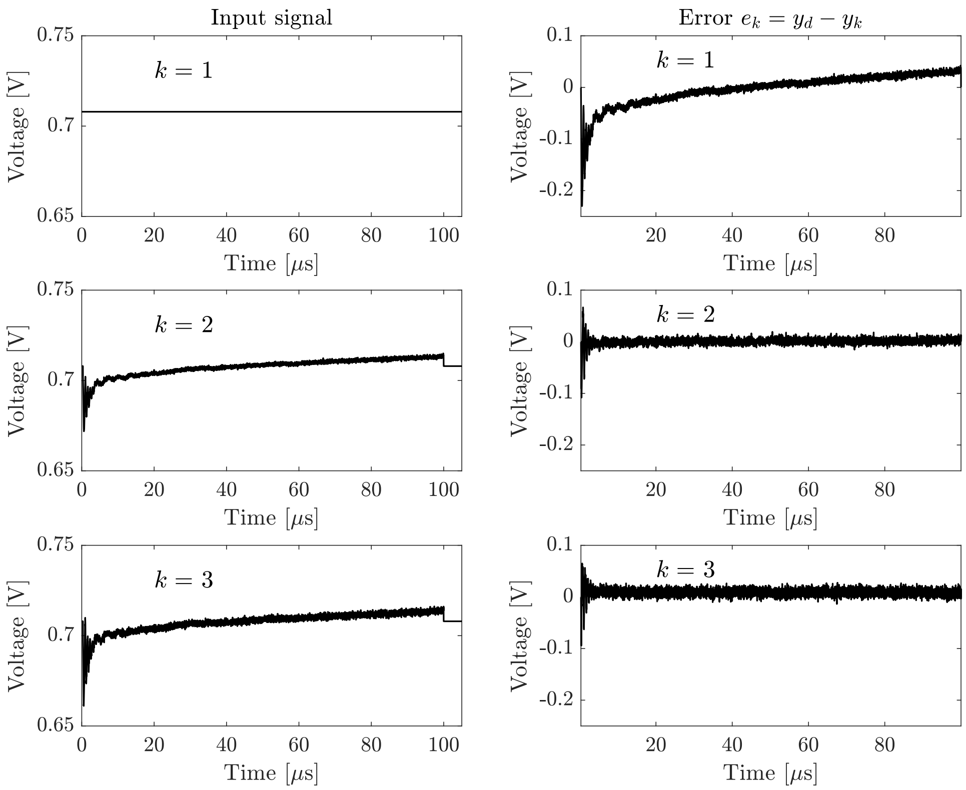

Figure 5.12: ILC in experiments for the 100 μs pulse, error observed between 0.33 and 99.99 μs. First column shows the input signal from ILC and second column shows the error achieved between the desired output and measured output.

6

Conclusion

This chapter will give a brief summary of the most important results and some conclusions that can be drawn will also be presented. Also a proposal for how the results from the research can be used in practical applications are given.

Measurements of the PA output in a transmitter have been performed, where the PA is turned off between the pulses. Two different PWs for the PA input have been used, 10 μs and 100 μs. The measurements showed that transients occur in the PA output when it is turned on, and also that a decaying behaviour occurs due to self heating, which was more apparent for the pulse with longer duration.

Black box modelling showed that different model structures are needed depending on PW of the input signal, except from the FIR model which achieved good performance for both pulses. Even though the PA has been operating in its linear regime, the 100 μs pulse needed a nonlinear Wiener model to achieve a good performance. For the shorter pulse, a linear OE model had good performance. The longer pulse includes more thermal memory effects, since the heat dissipation is increased when the PA is on for a longer period. By observing the static nonlinearity for the Wiener model one could see that it switched between three regions. One explanation for why a nonlinear model then is needed is that an increased amount of heating leads to a nonlinear gain of the amplifier. Other important characteristics that could be observed from the modelling is that the estimation of recursive models for the data are very sensitive to noise. When trying to directly estimate the models from one single measurement the simulated model did not follow the oscillations present in the measured output. It proved to be very successful to instead use the mean value from a set of measurements that had used the same input signal.

By studying partial transfer functions of for instance the OE models, one could see that two of the partial transfer functions seemed to cancel some of each others behaviour. Reducing the number of coefficients did not result in a good model. Hence it is of interest to investigate in the possibilities to apply other techniques to reduce the model order.

Implementation of DPD showed that it is possible to successfully compensate for all undesired memory effects in simulation. However, in experiments it was not possible to compensate for the oscillations in interval (c) in Figure 4.5 and 4.6. This was probably not achievable due to problems with timing of the instruments and unknown time delays. This problematic could already be seen in the initial measurements where each pulse did not start at the same time instance. This can be seen in Figure 3.4 and 3.5. From simulations it could be seen that in order to achieve a desired shape of the PA response, the input signal must be out of phase from the initial measured response. By ensuring perfect timing and gaining knowledge about the time delays until the trigger reaches the VSA and the pulse generator, it would probably be possible to also compensate also for this behaviour in experiments. From the measurements, it could be seen that the pulses started approximately after 0.15 μs. As explained in Chapter 3 about Measurements, a trigger from the VSG is sent both to the pulse generator and the VSA when a new period for the input signal is started. It is however known that there will be a short time delay until the VSA starts to measure and until the pulse generator turns the PA on. By adapting the input signal as shown in Figure 5.10 and Figure 5.12, it is assumed the VSA starts to measure directly and the PA is turned on after approximately 0.15 μs. However, the VSA most likely also introduces a delay and thereby the input signal must be shifted in time.

Also, it is desired to iteratively find the optimal input signal in simulation and thereafter apply that signal in experiments. However, the performance of the PA differs depending on the ambient temperature and if the PA has been used prior to the experiment. When the optimal input signal was found in simulation and applied in experiments, an offset in amplitude was present. This was probably due to a change in the ambient temperature from the initial measurements which the modelling were performed on to when the DPD was tested in the laboratory. Another possibility is that the PA might have been used prior to the DPD experiments which in turn changes the temperature of the device which affects the performance. Further improvement would instead have been achieved by either controlling the ambient temperature or by incorporating a temperature dependence in the modelling. Using an integrated temperature sensor on the device would enable the possibility to extend the modelling with a temperature dependence. Then the temperature can be measured before finding the optimal input signal in simulation.

When the offset in amplitude was observed, the approach used instead was to iteratively find the optimal input signal directly in experiments. The disadvantage with doing so is that the algorithm tries to compensate for the measurement noise as well, meaning that the input signal includes more noise for each iteration which leads to more noise in the measurement. One possible solution would be to low pass filter the data before it is used in the ILC.

With the ILC scheme, it is possible to offline iterate and find the optimal input signal that will result in a desired output response. Hence a suitable usage is to define pulse characteristics for a set of pulses, which depends on for instance desired detection range. Thereafter the corresponding optimal input signal for each pulse characteristic is found and can be saved in a look-up table. Hence no calculations will be needed in its practical implementation. Another possibility is to measure the PA output in the practical implementation. Thereby the input signal can be changed online such that the desired output signal is achieved. This however implies that it must be possible to measure the PA output.

7
Future work

There are several problems concerning modelling and measurements used for the design of DPD that remained unsolved and are therefore proposed as future research questions.

It was only investigated in when the PA was turned on with a constant RF signal. In order to have a full description of how the PA behaves, measurements of when the RF signal is varied are needed as well. Also measurements where the PA is turned on and the RF signal is varied simultaneously are needed. This might require a dual input model instead, where in this case it was possible to simplify it to a single input model.

The PA was also only operating in its linear regime. It is of interest to extend the work such that compensation of nonlinear distortion also is possible. The ILC algorithm would still be possible to use, but the model structures would need to be reconsidered.

Implementing the ILC in experiments did not successfully eliminate the oscillating transients that occurred when the PA was turned on. This was probably due to problems with unknown delays and timing of the instruments. From the initial measurements it could also be seen that the PA was not turned on at the exact same time instance for each measurement. Hence it is of interest to investigate in how the timing can be improved and to gain knowledge of the delays in the instruments which would give better result of the DPD.

It is also of interest to extend the work with a temperature dependence. In the conclusion it was discussed that the performance differs depending on temperature. If the practical implementation would be to save values of optimal input signals in a look-up table, the temperature also needs to be taken into consideration. A study of how sensitive the performance is to temperature changes is therefore needed and thereafter the modelling and design of DPD can be extended with a temperature dependence.

Bibliography

[1] C. Alabaster, *Pulse Doppler Radar.* GB: Institution Of Engineering & Technology (Iet), 2012.

[2] M. I. Skolnik, *Radar handbook*, 3rd ed. New York: McGraw-Hill, 2008.

[3] R. Stevenson, "Preparing gan for greater military service," *Compound Semicond.*, vol. 8, no. 5, pp. 30–34, 2013.

[4] C. F. Campbell, A. Balistreri, M. Kao, D. C. Dumka, and J. Hitt, "Gan takes the lead," *IEEE Microwave Magazine*, vol. 13, no. 6, pp. 44–53, 2012.

[5] C. G. Tua, "Measurement technique to assess the impact of rf power amplifier memory effects on radar performance," in *2012 IEEE Radar Conference*, May 2012, pp. 0089–0094.

[6] T. Thrivikraman, D. Perkovic-Martin, M. Jenabi, and J. Hoffman, "Radar waveform pulse analysis measurement system for high-power gan amplifiers," in *79th ARFTG Microwave Measurement Conference*, June 2012, pp. 1–4.

[7] S. Boumaiza and F. M. Ghannouchi, "Thermal memory effects modeling and compensation in rf power amplifiers and predistortion linearizers," *IEEE Transactions on Microwave Theory and Techniques*, vol. 51, no. 12, pp. 2427–2433, Dec 2003.

[8] A. Prejs, S. Wood, R. Pengelly, and W. Pribble, "Thermal analysis and its application to high power gan hemt amplifiers," in *2009 IEEE MTT-S International Microwave Symposium Digest*, June 2009, pp. 917–920.

[9] A. Rabany, N. Long, and D. Rice, "Memory effect reduction for ldmos bias circuits," *Microwave Journal*, vol. 46, no. 2, pp. 124–130, Feb 2003.

[10] O. Axelsson, S. Gustafsson, H. Hjelmgren, N. Rorsman, H. Blanck, J. Splettstoesser, J. Thorpe, T. Roedle, and M. Thorsell, "Application relevant evaluation of trapping effects in algan/gan hemts with fe-doped buffer," *IEEE Transactions on Electron Devices*, vol. 63, no. 1, pp. 326–332, Jan 2016.

[11] D. R. Morgan, Z. Ma, and L. Ding, "Reducing measurement noise effects in digital predistortion of rf power amplifiers," in *Communications, 2003. ICC '03. IEEE International Conference on*, vol. 4, May 2003, pp. 2436–2439 vol.4.

[12] J. C. Cahuana, *Digital Compensation Techniques for Power Amplifiers in Radio Transmitters.* Doktorsavhandlingar vid Chalmers tekniska högskola, 2017.

[13] C. G. Tua, T. Pratt, and A. I. Zaghloul, "A study of interpulse instability in gallium nitride power amplifiers in multifunction radars," *IEEE Transactions on Microwave Theory and Techniques*, vol. 64, no. 11, pp. 3732–3747, 2016.

[14] S. Boumaiza and F. M. Ghannouchi, "Thermal memory effects modeling and compensation in rf power amplifiers and predistortion linearizers," *IEEE Trans-*

actions on Microwave Theory and Techniques, vol. 51, no. 12, pp. 2427–2433, 2003.

[15] F. M. Ghannouchi, *Behavioral modeling and predistortion of wideband wireless transmitters*, 1st ed. Chichester, West Sussex, United Kingdom: Wiley, 2015.

[16] M. Isaksson, D. Wisell, and D. Ronnow, "A comparative analysis of behavioral models for rf power amplifiers," *IEEE Transactions on Microwave Theory and Techniques*, vol. 54, no. 1, pp. 348–359, Jan 2006.

[17] B. Mulgrew, P. M. Grant, and J. Thompson, *Digital signal processing: concepts and applications*, 2nd ed. Basingstoke: Palgrave Macmillan, 2003.

[18] R. Johansson, *System modeling and identification.* Englewood Cliffs, N.J: Prentice Hall, 1993.

[19] C. Eun and E. J. Powers, "A new volterra predistorter based on the indirect learning architecture," *IEEE Transactions on Signal Processing*, vol. 45, no. 1, pp. 223–227, Jan 1997.

[20] P. N. Landin, A. E. Mayer, and T. Eriksson, "Mila - a noise mitigation technique for rf power amplifier linearization," in *2014 IEEE 11th International Multi-Conference on Systems, Signals Devices (SSD14)*, Feb 2014, pp. 1–4.

[21] J. Chani-Cahuana, P. N. Landin, C. Fager, and T. Eriksson, "Iterative learning control for rf power amplifier linearization," *IEEE Transactions on Microwave Theory and Techniques*, vol. 64, no. 9, pp. 2778–2789, Sept 2016.

A

Models and measurements

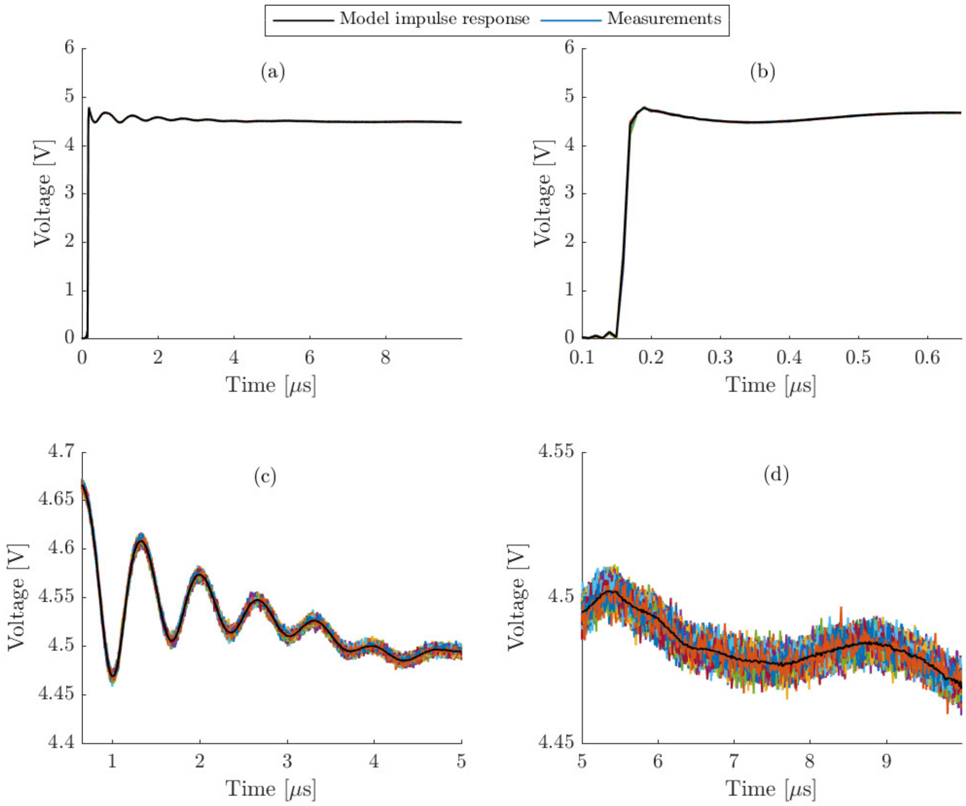

Figure A.1: Simulated FIR model for the 10 μs pulse together with measurement data for 100 pulses divided into the four evaluation intervals.

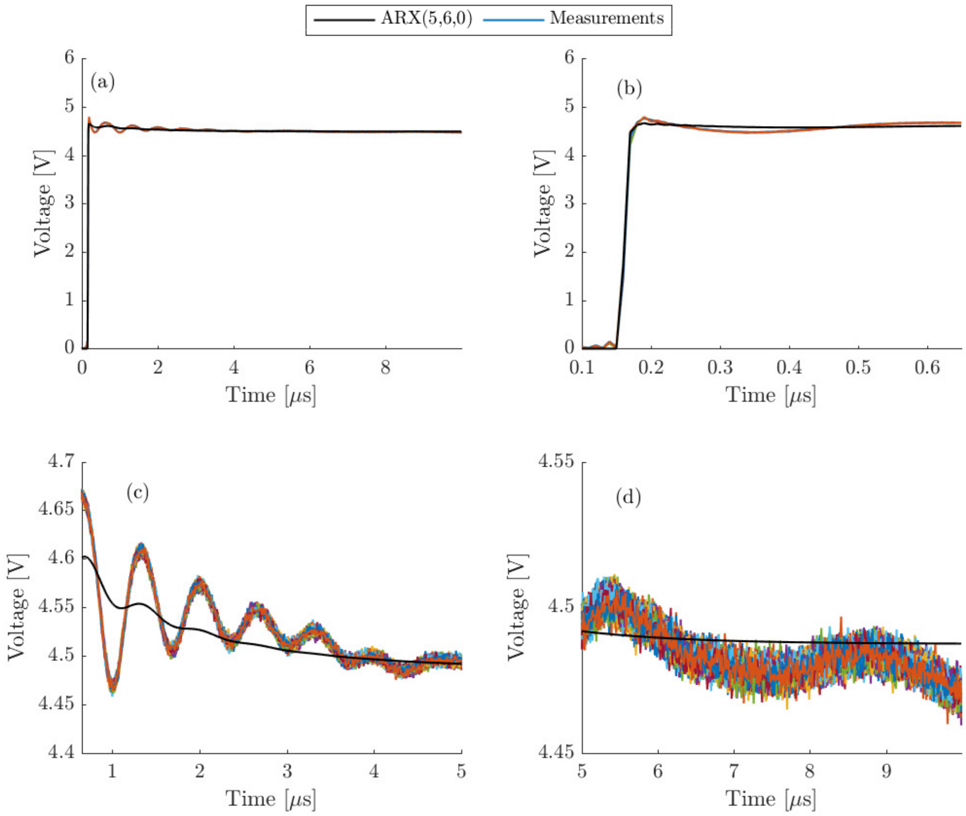

Figure A.2: Simulated ARX(5,6,0) for the 10 μs pulse together with measurement data for 100 pulses divided into the four evaluation intervals.

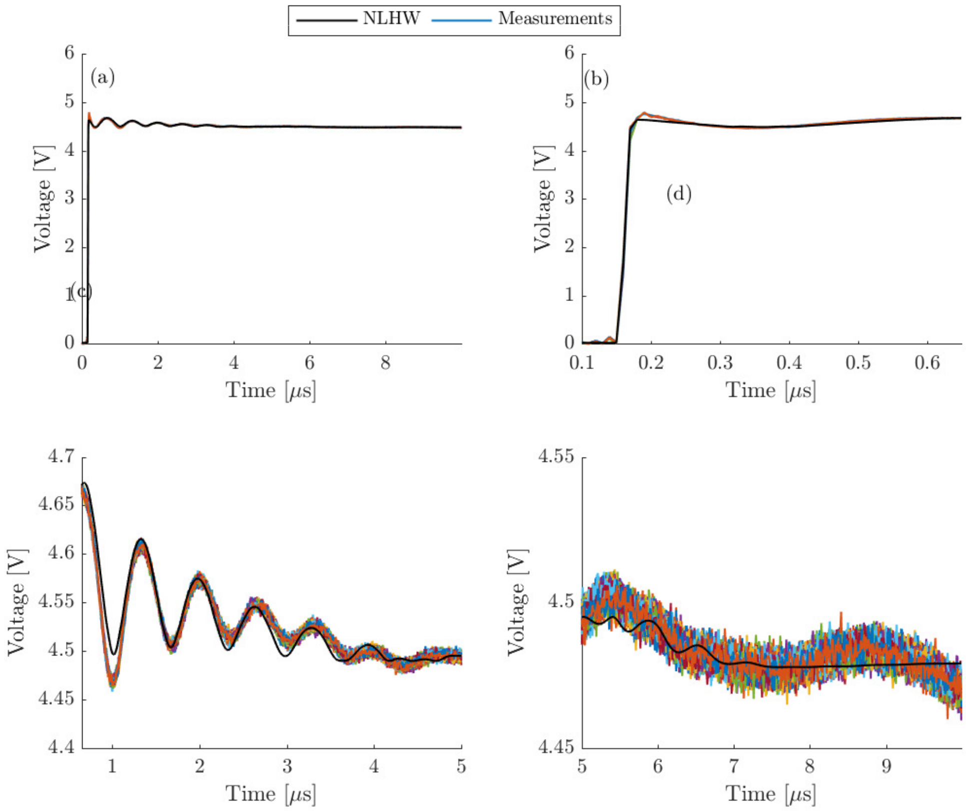

Figure A.3: Simulated Wiener model for the 10 μs pulse together with measurement data for 100 pulses divided into the four evaluation intervals.

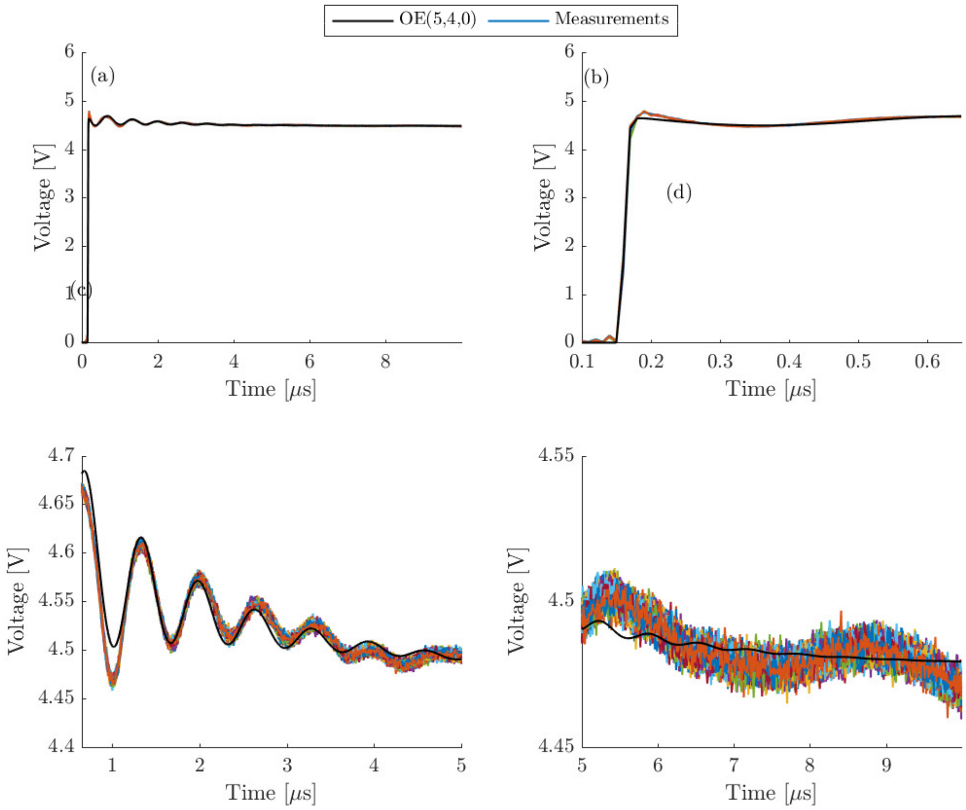

Figure A.4: Simulated OE(5,4,0) for the 10 μs pulse together with measurement data for 100 pulses divided into the four evaluation intervals.

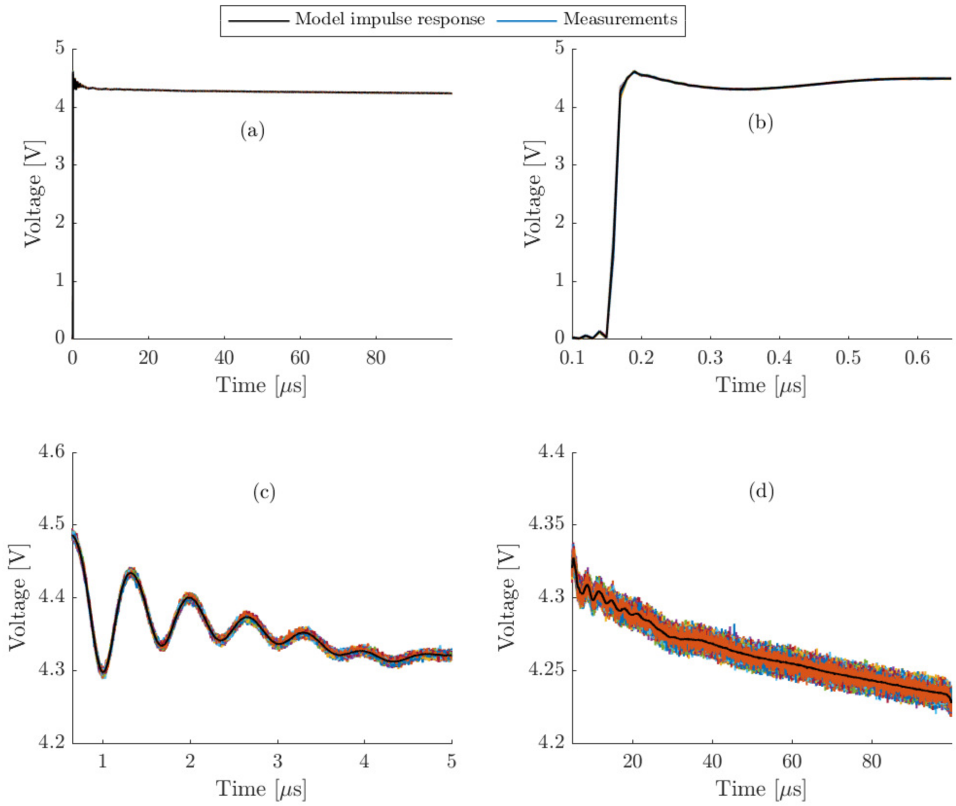

Figure A.5: Simulated FIR model for the 100 μs pulse together with measurement data for 100 pulses divided into the four evaluation intervals.

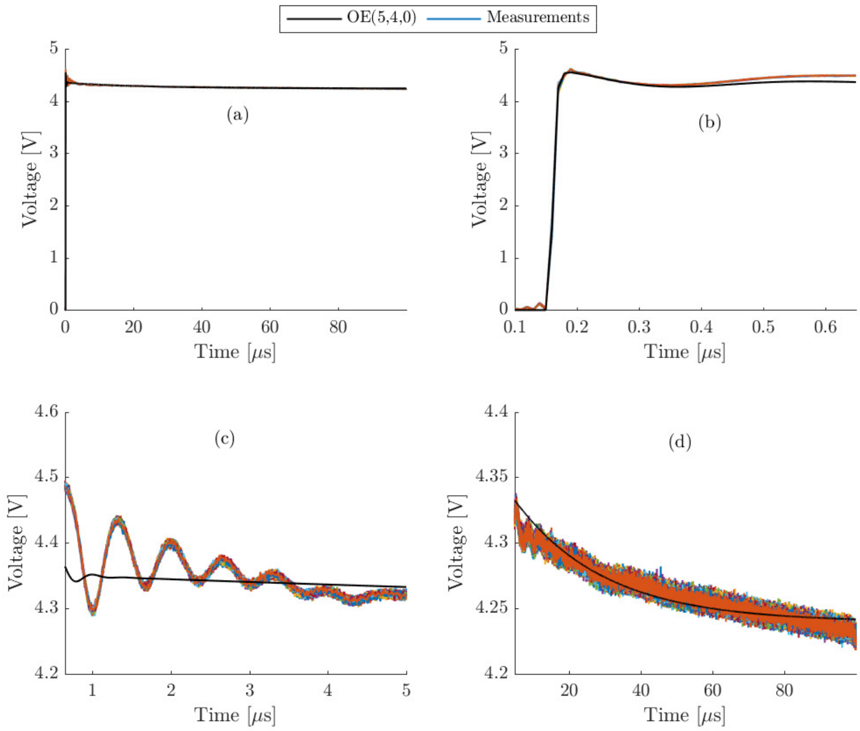

Figure A.6: Simulated OE(5,4,0) for the 100 μs together with measurement data for 100 pulses divided into the four evaluation intervals.

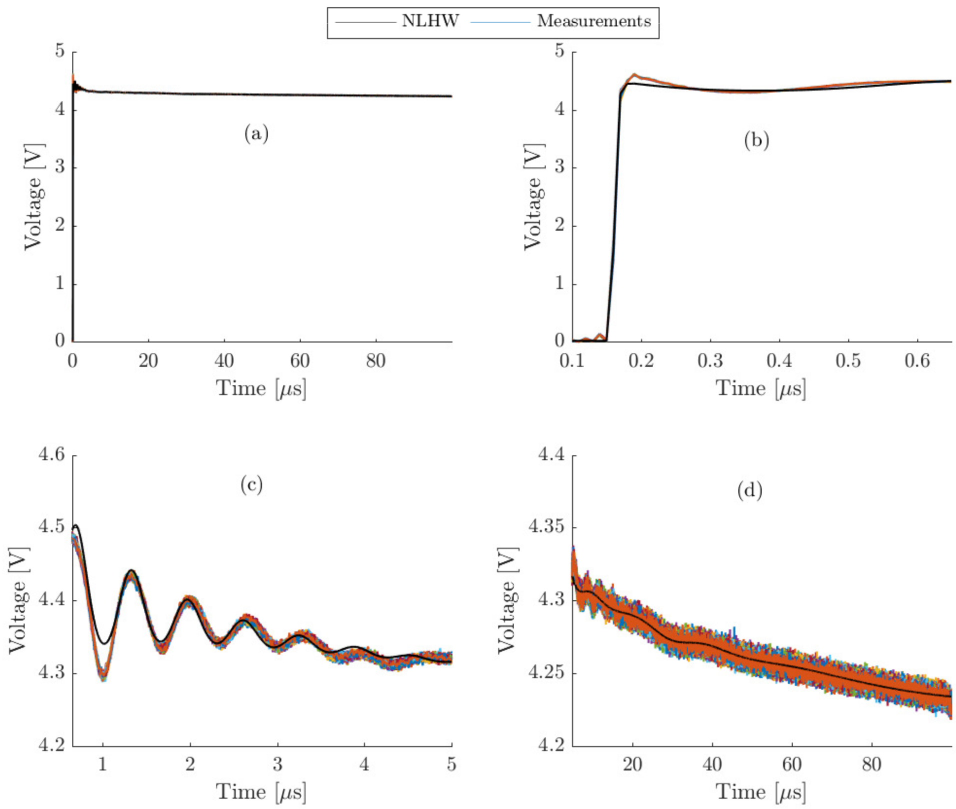

Figure A.7: Simulated Wiener model for the 100 μs pulse together with measurement data for 100 pulses divided into the four evaluation intervals.